2012

Experimental and analytical trajectories of simplified debris models in tornado winds

Kristin Crawford
Iowa State University

Experimental and analytical trajectories of simplified debris models in tornado winds

by

Kristin Leigh Crawford

A thesis submitted to the graduate faculty

in partial fulfillment of the requirements for the degree of

MASTER OF SCIENCE

Major: Aerospace Engineering

Program of Study Committee:
Partha P. Sarkar, Major Professor
Fred Haan
Peter Sherman

Iowa State University

Ames, Iowa

2012

TABLE OF CONTENTS

LIST OF TABLES ..... **v**

LIST OF FIGURES ..... **vi**

ACKNOWLEDGEMENTS ..... **x**

ABSTRACT ..... **xi**

CHAPTER 1. GENERAL INTRODUCTION AND BACKGROUND **1**

1.1 INTRODUCTION 1

1.2 BACKGROUND 1

1.3 OBJECTIVE AND MOTIVATION FOR CURRENT RESEARCH 3

1.4 THESIS ORGANIZATION 4

CHAPTER 2. EXPERIMENTAL METHODOLOGY **6**

2.1 STEREO-PHOTOGRAMMETRY 6

2.1.1 Introduction 6

2.1.2 Validation of Stereo-Photogrammetry Technique 8

2.1.3 Scaling of Debris Objects 12

2.1.4 Experimental Setup 15

2.2 DEBRIS AERODYNAMIC COEFFICIENTS 19

2.2.1 Sphere Force Coefficients 19

2.2.2 Cylinder Force And Moment Coefficients 20

CHAPTER 3. NUMERICAL METHODOLOGY 28

3.1 PREDICTION OF TORNADIC WIND VELOCITY TIME HISTORIES 28

3.2 TRAJECTORY PROPAGATION METHODOLOGY 33

3.2.1 Introduction 33

3.2.2 Sphere 34

3.2.2.1 Overview of Forces 34

3.2.2.2 Validation of Sphere Forces 37

3.2.3 Circular Cylinder 40

3.2.3.1 Overview of Forces And Moments 40

3.2.3.2 Validation of Cylinder Forces 46

CHAPTER 4. RESULTS AND DISCUSSION 50

4.1 COMPARISON OF EXPERIMENTAL AND NUMERICAL TRAJECTORIES 50

4.1.1 Sphere 50

4.1.2 Cylinder 55

4.2 DISCUSSION OF RESULTS 58

CHAPTER 5. CONCLUSION 61

5.1 SUMMARY AND CONCLUSIONS OF CURRENT WORK 61

5.2 RECOMMENDATIONS FOR FUTURE RESEARCH 63

APPENDIX A. STEREO-PHOTOGRAMMETRY TRAJECTORIES 64

APPENDIX B. COEFFICIENTS OF CIRCULAR CYLINDER 67

APPENDIX C. VELOCITY AND PRESSURE MEASUREMENT PLOTS 68

BIBLIOGRAPHY 70

LIST OF TABLES

Table 2.1 Swirl ratios for various vane settings (Haan et al., 2008) 9

Table 2.2 Results of stereo-photogrammetry validation test using 3:1 cylinder 12

Table 2.3 Enhanced Fujita scale 14

Table 2.4 Scaling parameters and prototype properties for models used in tornado simulator 15

Table 2.5 Debris trajectory test descriptions 15

Table 3.1 Constants for different radial velocity curves 31

Table 3.2 Results of the sphere forces validation test 40

Table 3.3 Results of the cylinder forces validation test 48

Table 4.1 Trajectory comparisons for Test 1 51

Table 4.2 Trajectory comparisons for Test 2 52

Table 4.3 Trajectory comparisons for Test 3 53

Table 4.4 Trajectory comparisons for Test 4 54

Table 4.5 Trajectory comparisons for Test 5 56

Table 4.6 Trajectory comparisons for Test 6 57

LIST OF FIGURES

Figure 1.1 Examples of tornado-generated debris 2

Figure 2.1 Stereo-photogrammetry setup 6

Figure 2.2 Stereo-photogrammetry validation test 8

Figure 2.3 Stereo-photogrammetry grid shown for both cameras in validation test 10

Figure 2.4 Stereo-photogrammetry grid and cylinder trajectory in pixels for validation test 11

Figure 2.5 Results of stereo-photogrammetry validation test 12

Figure 2.6 Debris objects used in tornado simulator 13

Figure 2.7 Sphere debris initial conditions 16

Figure 2.8 Initial placement of debris objects 17

Figure 2.9 Stereo-photogrammetry grid as seen in Camera 1 in the tornado simulator and in pixels 17

Figure 2.10 Stereo-photogrammetry grid as seen in Camera 2 in the tornado simulator and in pixels 17

Figure 2.11 Trajectory for Test 2 in pixels as seen for Camera 1 (left) and Camera 2 (right) 18

Figure 2.12 Stereo-photogrammetry trajectory, Test 2 (Table 2.5) 18

Figure 2.13 Coefficient of drag, C_D, for sphere versus Reynolds number (Blevins et. al., 1992) 19

Figure 2.14 Digitized points of Coefficient of drag, C_D, for sphere versus Reynolds number 20

Figure 2.15 Aerodynamic force and moment coefficients on a circular cylinder 21

Figure 2.16 Experimental setup for measuring aerodynamic coefficients of circular cylinder 21

Figure 2.17 Depiction of yaw (μ) and pitch (θ) angles 22

Figure 2.18 Force-balance and force-balance-translated coordinate systems 22

Figure 2.19 Principle coordinate system 23

Figure 2.20 Relationship between force-balance-translated and principle coordinate systems 23

Figure 2.21 Yaw rotation (μ) about '$\boldsymbol{z}*$' axis. 24

Figure 2.22 Pitch rotation (θ) about '$\boldsymbol{y'}$' axis. 24

Figure 3.1 Normalized V_θ measurements to determine core radius r_c of 'Vane 5' setting (Haan et al., 2008) at z = 31.8 mm height 28

Figure 3.2 Normalized V_θ profile for 'Vane 5' setting (Haan et al., 2008) 30

Figure 3.3 Normalized V_r profiles at four radial distances for 'Vane 5' setting (Haan et al., 2008) 31

Figure 3.4 V_z data taken at various height, *z*, and radius, *r*, locations 32

Figure 3.5 Tornadic wind velocity components and corresponding angles 32

Figure 3.6 Forces acting on sphere in three-dimensional flow 34

Figure 3.7 Static pressure measurements as function of radius from vortex center for 'Vane 5' setting 35

Figure 3.8 Incremental pressure force, $dF_{p,r}$, acting on a small section of the sphere 36

Figure 3.9 Forces acting on a sphere in the validation test 38

Figure 3.10 Relationship between principle and global coordinate systems 41

Figure 3.11 Total velocity components and corresponding angles in global coordinate system 41

Figure 3.12 Orientation of the cylinder with respect to direction of the magnitude of the total velocity vector, U 43

Figure 3.13 Forces acting on circular cylinder in three-dimensional flow 44

Figure 3.14 Forces acting on a cylinder in the validation test 47

Figure 4.1 Comparison of experimental vs. numerically simulated sphere trajectory, Test 1 (r_0 = 305mm, h_0 = 279.5mm) 51

Figure 4.2 Comparison of experimental vs. numerically simulated sphere trajectory, Test 2 (r_0 = 381mm, h_0 = 279.5mm) 52

Figure 4.3 Comparison of experimental vs. numerically simulated sphere trajectory, Test 3 (r_0 = 381mm, h_0 = 152.5mm) 53

Figure 4.4 Comparison of experimental vs. numerically simulated sphere trajectory, Test 4 (r_0 = 305mm, h_0 = 152.5mm) 54

Figure 4.5 Comparison of experimental vs. numerically simulated sphere trajectory, Test 5 (r_0 = 254mm, h_0 = 152.5mm) 56

Figure 4.6 Comparison of experimental vs. numerically simulated sphere trajectory, Test 6 (r_0 = 254mm, h_0 = 152.5mm) 57

Figure 4.7 Turbulence intensity of total velocity component for ‘Vane 5’ setting 58

Figure A.1 Stereo-photogrammetry trajectory, Test 1 64

Figure A.2 Stereo-photogrammetry trajectory, Test 2 64

Figure A.3 Stereo-photogrammetry trajectory, Test 3 65

Figure A.4 Stereo-photogrammetry trajectory, Test 4 65

Figure A.5 Stereo-photogrammetry trajectory, Test 5 66

Figure A.6 Stereo-photogrammetry trajectory, Test 6 66

Figure A.7 Coefficients of circular cylinder, calculated from data collected in Bill James Wind Tunnel 67

Figure A.8 Pressure and velocity measurements for swirl ratio = 0.08 and height z = 0.762 m 68

Figure A.9 Pressure and velocity measurements for swirl ratio = 0.08 and height z = 1.016 m 69

Figure A.10 Pressure and velocity measurements for swirl ratio = 0.24 and height z = 0.762 m 69

ACKNOWLEDGEMENTS

First and foremost I would like to thank God, for without him nothing is possible. I owe my deepest gratitude to my amazing parents, sister and boyfriend for their love and encouragement. Their never-ending support constantly renewed my determination to complete my master's program. I would also like to thank my grandparents and friends for their prayers and support. Thanks go to my major professor, Dr. Partha P. Sarkar, and other members of my committee, Dr. Fred Haan and Dr. Peter Sherman, for their help and guidance along the way. Thanks to Bill Rickard and his staff for their assistance and inspiration in the WiST laboratory. I would also like to thank all the faculty and staff at the Department of Aerospace Engineering.

ABSTRACT

Wind-borne debris is considered as a major source of damage to civil structures during strong wind storms such as hurricanes and tornadoes. After wind-induced failure, building components can become airborne as missiles and cause significant damage to the surrounding structures. Similarly, any loose or broken object such as roof gravel, a tree limb, or a vehicle that becomes airborne could do substantial damage to building cladding. There are various studies to model simplified wind-borne debris in flight to predict its trajectory and maximum speed in straight-line wind. There has been little research modeling wind-borne debris in three-dimensional wind flow of a tornado. Maruyama (2011) used a numerically generated tornado to model the trajectory of a simplified debris that represents a "compact" object in which dynamic equations of motion of the missile were greatly simplified and a majority of the force characteristics of the object in flight were neglected. In the current study, ISU's tornado simulator was used to validate a quasi-steady numerical model used to simulate free-flight trajectories of two types of wind-borne debris. The coordinates of the trajectories in the experiments were captured using two cameras and the principles of stereo-photogrammetry. The experimental trajectories were compared to a numerical simulation model that used the tornado wind flow parameters based on empirical models of measured velocity profiles and aerodynamic properties such as force and moment coefficients of the selected debris shape as measured in the Bill James Wind Tunnel. The wind-borne debris models that were used for validation were (a) two spheres of diameter

25.4 mm (1.0 inch) and 38.1 mm (1.5 inches) and masses 0.19 g and 0.77 g and (b) two cylinders with an aspect ratio of 3:1 (length:diameter) with diameter 12.7 mm (0.5 inch) and 25.4 mm (1 inch), lengths 38.1 mm (1.5 inches) and 76.2 mm (3 inches) and masses 0.09 g and 0.60 g, respectively. The sphere debris objects were representative of (compact) objects with similar dimensions along all three coordinate directions, and the cylindrical debris objects were representative of 2x4 inch timber planks and a light-weight vehicle when scaled to full-size using Tachikawa scaling. The comparison between the observed- and numerically-simulated trajectories for both the sphere and cylinder in controlled-flight condition was excellent and thereby it validated the equations used to model the forces acting on the objects. A constant acceleration integration method was used to propagate the free-flight trajectories of the debris objects. In the numerically-simulated free-flight trajectory of the cylinder, the effects of moment and angular accelerations were neglected to simplify the equations of motion. The error between the observed- and numerically-simulated trajectories for both the sphere and cylinder in free-flight was low at the beginning of flight and increased with time. The prediction of trajectory for both objects can be further improved by including turbulence in the velocity model used and modeling the second-order force effects. The trajectory predictions for the cylinder can also be substantially improved by considering the rotational components of its motion in free flight.

CHAPTER 1. GENERAL INTRODUCTION AND BACKGROUND

1.1 INTRODUCTION

Wind-borne debris is considered a major source of damage during strong wind storms such as hurricanes and tornadoes. After wind-induced failure, building components can become airborne as missiles and cause significant damage to the surrounding structures. Debris trajectory in straight-line wind has been extensively studied and understood, but research on understanding of near-ground flow field in tornados and their effect on man-made structures is a relatively new field.

1.2 BACKGROUND

Over the past three decades there have been many studies on the trajectory of flying debris pioneered through the extensive research in the area of plate-type debris by Tachikawa et al. (1983). Wills et al. (2002) characterized wind-borne debris by shape and aerodynamic properties into three groups: compact, plate-like, and rod-like. Holmes et al. (2006) and Baker et al. (2007) applied model equations to predict horizontal flight speeds in uniform 2-D flow for applications to impact testing. Kordi et al. (2009) showed that the buoyancy parameter, rotational drag, and initial launch conditions significantly affect the flight path of flat plates in a uniform 2-D flow. However, there has been little research in the area of three-dimensional flow, such as in tornado or hurricane-type winds. Maruyama (2011) used Large

Eddy Simulation to numerically calculate various tornado-like vortices and model the trajectories of a simplified debris “compact” object. Much care was taken to create the numerical tornado simulator but the equations of motion of the debris object were greatly simplified. The majority of the aerodynamic forces acting on the object, including buoyancy, force due to centripetal acceleration, and pressure force, were neglected. Kordi et al. (2009) showed that in quasi-steady theory for the flight of wind-borne plate debris in uniform flow, the buoyancy parameter is not insignificant and should be included in the equations of motion.

Field studies and aerial photos of tornado damage path show that tornado-generated missiles can vary from small roof gravel, causing mostly broken window glass, up to incredible missiles such as automobiles, railroad cars, and large storage tanks as shown in Figure 1.1.

Figure 1.1 Examples of tornado-generated debris

The most common types of tornado-generated missiles are 2x4 inch timber planks weighing 12-15 lb from damaged or destroyed wood frame houses. Individual planks have been observed to penetrate walls and roofs and impale the ground, McDonald (1990). Compressed air cannons (such as the air-actuated cannon in the Tornado Missile Impact Facility at Texas Tech University) can easily propel a representative debris object such as 2x4 timber plank to speeds of up to 150 mph for uses in impact testing of walls, shutters, and windows, Minor (1994).

Research on understanding of flow field in tornados and their effect on man-made structures is a relatively new field. Haan et al. (2008) used ISU's Tornado Simulator to experimentally simulate tornado-like vortices for the purpose of understanding tornado-induced loads on various low-rise structures. There has been little investigation into the tornado-induced motion of non-stationary objects, such as debris trajectories.

1.3 OBJECTIVE AND MOTIVATION FOR CURRENT RESEARCH

In view of these past studies, the following research tasks were proposed:

1. Develop a methodology using dynamic equations of motion to numerically compute the trajectory of a debris object of a finite shape and validate it using laboratory measurements in the ISU Tornado Simulator. The model should take into account all the forces acting on the object in a simulated tornado. The debris objects that were selected for laboratory testing are spheres of two different sizes, representative of compact objects in the field, and circular cylinders of two different sizes with an aspect ratio (length:diameter) of 3:1, representative of elongated objects such as a tank, silo, or vehicle.

2. In order to compare the numerically simulated trajectories based on the analytical model developed to the experimental ones, a stereo-photogrammetry method must be developed and validated to extract three-dimensional coordinates of the experimentally simulated trajectories in the ISU Tornado Simulator.

This work was motivated by the need to predict the trajectories of windborne debris in tornado-like winds. If the trajectory, velocity, and orientation of the object along its path can be predicted using numerical models, damage of various targeted structures and injury can possibly be mitigated.

1.4 THESIS ORGANIZATION

The studies herein focus on two ways of examining the wind-borne debris. The second chapter of this thesis contains details of the stereo-photogrammetry method developed in order to extract three-dimensional coordinates of the experimental debris trajectories in ISU's Tornado Simulator. This chapter also includes details on wind-tunnel testing in ISU's Bill James Wind Tunnel for the purpose of extracting the aerodynamic force and moment coefficients for a circular cylinder of aspect ratio 3:1. The third chapter presents the analytical simulation of the debris trajectories. This includes the development and validation of the equations of motion for both the sphere and circular cylinder and details of the calculation of motion based on a quasi-steady approach. The model of the velocity field in the tornado simulator is also described in this chapter. Comparisons of the experimental trajectories and analytical simulation are presented in the fourth chapter. A discussion follows that explains the outcomes and implications of the research. A conclusion and recommendations for future work are included in the fifth and final chapter. An appendix at

the end of the thesis contains figures that are referenced in the previous chapters. All numerical simulations reported in this thesis were performed using MATLAB software.

CHAPTER 2. EXPERIMENTAL METHODOLOGY

2.1 STEREO-PHOTOGRAMMETRY

2.1.1 Introduction

In this work, ISU's Tornado Simulator was used to experimentally validate the numerically simulated trajectory of various types of wind-borne debris in a representative wind-field of a tornado. Therefore, the three-dimensional coordinates of the debris objects' trajectories inside the tornado simulator had to be recorded. The coordinates of the trajectory in the experiment were captured using two cameras and principles of stereo-photogrammetry. Two cameras were placed at a known distance *d* from each other and *l* from a background grid, as shown in Figure 2.1.

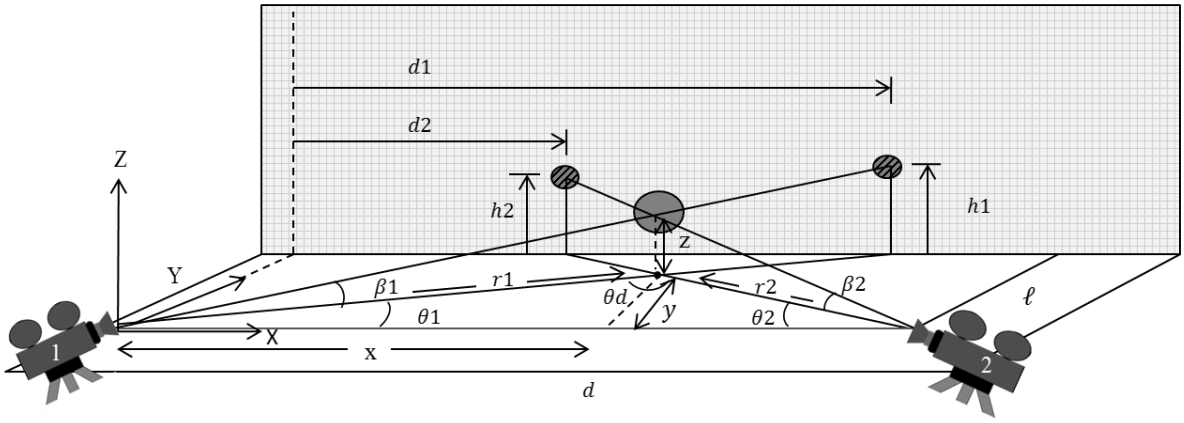

Figure 2.1 Stereo-photogrammetry setup

For every frame, *d* and *l* were constants and known. Each camera recorded the grid points of the object that it "sees", i.e. *d1, h1, d2, h2,* and from those the (x,y,z) coordinates of the

object with respect to the origin located at camera 1 could be calculated. The system was over-defined having four inputs for three outputs, but the equations were solved using (*d1, d2, h1*) and (*d1, d2, h2*) separately and averaging the respective (x,y,z) coordinates. The following equations were used to solve for the (x,y,z) coordinates of the object.

$$\theta 1 = tan^{-1}\left(\frac{\ell}{d1}\right) \quad \text{Equation 2.1}$$

$$\theta 2 = tan^{-1}\left(\frac{\ell}{d - d2}\right) \quad \text{Equation 2.2}$$

$$\theta d = \pi - (\theta 1 + \theta 2) \quad \text{Equation 2.3}$$

$$\beta 1 = tan^{-1}\left(\frac{h1}{\sqrt{\ell^2 + d1^2}}\right) \quad \text{Equation 2.4}$$

$$r1 = \frac{d}{sin(\theta d)} sin(\theta 2) \quad \text{Equation 2.5}$$

$$\beta 2 = tan^{-1}\left(\frac{h2}{\sqrt{\ell^2 + (d - d2)^2}}\right) \quad \text{Equation 2.6}$$

$$r2 = \frac{d}{sin(\theta d)} sin(\theta 1) \quad \text{Equation 2.7}$$

$$x = \frac{r1\, cos(\theta 1) + d - r2\, cos(\theta 2)}{2} \quad \text{Equation 2.8}$$

$$y = \frac{r1\, sin(\theta 1) + r2\, sin(\theta 2)}{2} \quad \text{Equation 2.9}$$

$$z = \frac{r1\, tan(\beta 1) + r2\, tan(\beta 2)}{2} \quad \text{Equation 2.10}$$

Adjustments had to be made in the equations when $d1 < 0$ in order to make sure that $\theta 1 > \frac{\pi}{2}$. The same was true when $d2 > d$ in order to make sure that $\theta 2 > \frac{\pi}{2}$. This was done by simply adding $\frac{\pi}{2}$ to the appropriate $\theta 1$ or $\theta 2$ equation. Appropriate values were then added to the coordinates (x,y,z) in order to center the coordinate system at the center of the tornado vortex on the simulator ground plane.

2.1.2 Validation of Stereo-Photogrammetry Technique

In order to validate the equations of the stereo-photogrammetry for use in the tornado simulator, an experimental setup was used as shown in Figure 2.2. When an object is hung by a string from the center of the tornado simulator, the object reaches an equilibrium spinning at a fixed r and h depending on the object properties, length *l* of the string, and the flow-field of the tornado-like vortex. The height *h* at which the object spins can be measured manually inside the simulator, and the radius *r* can be calculated from *h* and *l* (Figure 2.2).

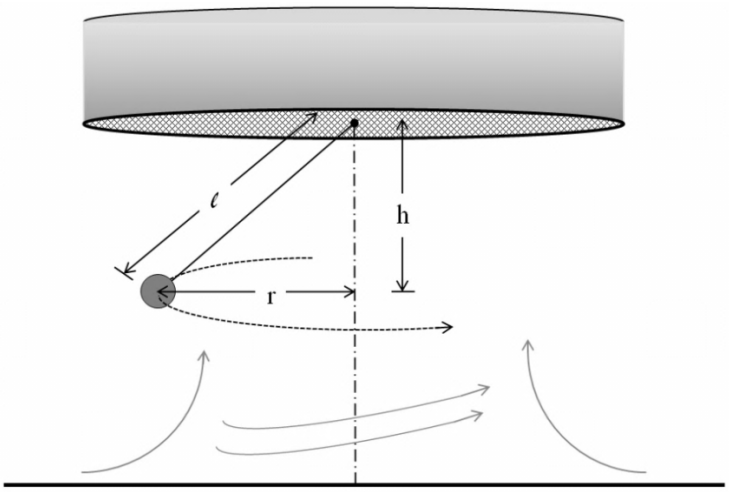

Figure 2.2 Stereo-photogrammetry validation test

The goal in this validation test was to accurately measure via stereo-photogrammetry the height and radius at which an object was in equilibrium for various swirl ratios of the tornado-like vortex. The swirl ratio is a common dimensionless flow parameter used to characterize the relative amount of angular to radial momentum in a vortex. Swirl ratio *S*, as calculated at the radius of the core r_c, is given by Equation 2.11.

$$S = \frac{r\Gamma}{2Q} = \frac{\pi r_c^2 V_{\theta_{max}}}{Q} \qquad \text{Equation 2.11}$$

In this equation, *r* is the radial distance from the center of the vortex to the point where *S* is calculated, Γ is circulation at *r*, $V_{\theta_{max}}$ is the maximum tangential wind speed, and Q is the volume inflow rate. Q was estimated as Q_{Fan} which is the flow rate through the duct housing of the fan.

The experiments were performed using simulated tornadoes with 'Vane 1' and 'Vane 3' settings (Haan et al., 2008). The vane settings refer to specific 'vane angle' settings in the tornado simulator to generate a tornado vortex of a specific vortex structure. Vane settings and corresponding swirl ratios are given in Table 2.1.

Table 2.1 Swirl ratios for various vane settings (Haan et al., 2008)

Case	r_c (m)	$V_{\theta,max}$ (m/s)	Q (m^3/s)	S at r_c
Vane 1	0.23	6.9	14.4	0.08
Vane 3	0.30	9.7	11.5	0.24
Vane 5	0.53	9.7	7.6	1.14

Relatively low swirl ratios were used for these tests because it has been reported that vortex simulations with swirl ratios below 0.5 produce "one-celled" vortices (Davies-Jones, 1973). These one-celled vortices are associated with single, narrow axisymmetrical vortices in

which the flow is relatively constant and less turbulent. This makes it easier for the debris object to reach steady equilibrium above the ground floor plane at a certain *r*. However it needs to be clarified that the stereo-photogrammetry tests can be used in any swirl ratio as long as the object is always viewable by both cameras.

A setup similar to Figure 2.1 was used in the ISU Tornado Simulator. Two identical high definition cameras with frame rates of 30Hz were used in this study. They were placed at a distance of d = 1.5 m apart and l = 4.2 m from the grid. Camera 1 was centered at 0.254 m inwards from the left edge of the grid (1.905x1.016 m). The origin centered at Camera 1 was 0.14 m above the floor plane and (x,y) = (-0.89,-3.0) m from the center of the tornado vortex. Figure 2.3 shows the grid image each camera captures.

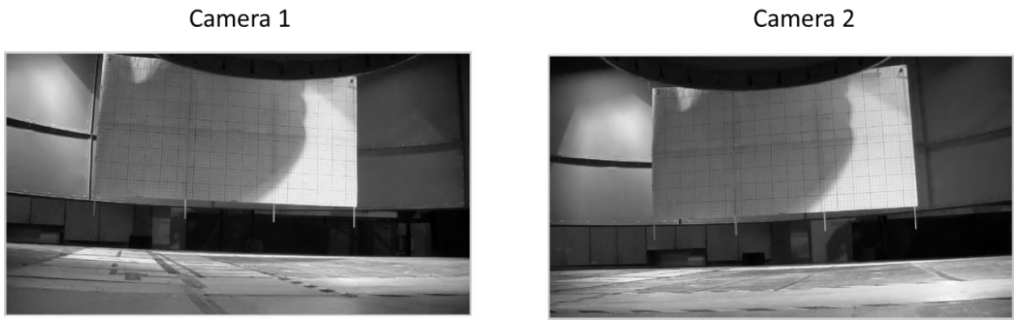

Figure 2.3 Stereo-photogrammetry grid shown for both cameras in validation test

First, the pixel locations of the grid points were found for each camera. Then the grid was removed and the experiment was performed. The camera images were matched up by turning a light on and off that could be seen by both cameras. The image where the light was first turned off synchronized the camera images. For this experiment, a light-weight circular cylinder of aspect ratio 3:1 was suspended by a string from the center of the tornado simulator as described in Figure 2.1. The trajectory was recorded once every 5 frames (for

frames per second of 30Hz, this is once every 0.167 seconds) for a total of approximately 3 revolutions of the cylinder. The trajectory of the top of the cylinder was found in pixels and is shown in Figure 2.4. The small dots in this figure represent the grid points (every 0.127 m) and the open circles represent the object's trajectory.

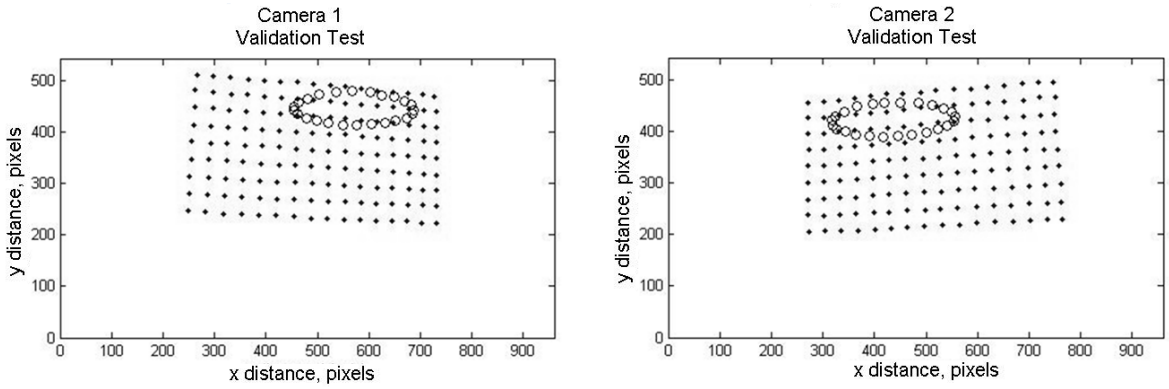

Figure 2.4 Stereo-photogrammetry grid and cylinder trajectory in pixels for validation test

The grid points in meters were known with respect to Camera 1. Therefore, the trajectory coordinates (*d1*, *d2*, *h1*, and *h2* from Figure 2.1) in meters on the grid were determined manually using the pixel locations of the trajectory with respect to the pixel locations of the grid points. The photogrammetry calculations were performed using the grid point coordinates for each camera and the three-dimensional coordinates of the trajectory were found. The (x,y,z) coordinates from the stereo-photogrammetry calculations were centered at Camera 1, as previously noted. The coordinates were transformed to a tornado simulator-centered coordinate system, where the origin lies at the center of the tornado vortex on the ground plane. Figure 2.5 shows the stereo-photogrammetry results from the validation experiment.

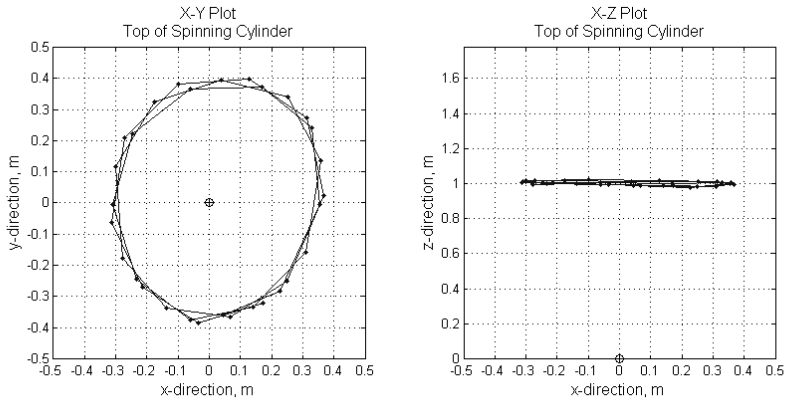

Figure 2.5 Results of stereo-photogrammetry validation test

The average height, *h*, and radius, *r*, from Figure 2.1 are shown in Table 2.2 where stereo-photogrammetry values are compared with the measured values. The small difference between calculated values from stereo-photogrammetry and the measured values leads to the conclusion that the stereo-photogrammetry setup and equations work very well for calculating the three-dimensional coordinates of objects moving in the tornado simulator.

Table 2.2 Results of stereo-photogrammetry validation test using 3:1 cylinder

	Measured values	Stereo-photogrammetry values	Percent difference
Height off ground, *h* (mm)	965	973	0.83
Radius, *r* (mm)	363	371	2.20

2.1.3 Scaling of Debris Objects

The wind-borne debris models tested in the tornado simulator were (a) two spheres of different diameters and masses representative of compact objects in the field with similar dimensions, and (b) two cylinders of different diameters and masses with an aspect ratio of

3:1 (length to diameter) which is representative of a silo, tank, vehicle or any other elongated object. The objects used are shown in Figure 2.6. The spheres were of diameter 25.4 mm (1.0 inch) and 38.1 mm (1.5 inches) and masses 0.19 g and 0.77 g, respectively. The cylinders were of diameter 12.7 mm (0.5 inch) and 25.4 mm (1 inch), lengths 38.1 mm (1.5 inches) and 76.2 mm (3 inches) and masses 0.09 g and 0.60 g, respectively.

Figure 2.6 Debris objects used in tornado simulator

Tachikawa was a pioneer in the study of wind-borne debris through his extensive research in the area of plate-type debris trajectories (Tachikawa, 1983). One of his most significant contributions was the Tachikawa number, K, a non-dimensional ratio of aerodynamic forces to gravity forces characterized by Equation 2.12.

$$K = \frac{\rho_{air} V^2 A}{2mg} \qquad \text{Equation 2.12}$$

In this study, the scaling of the model and prototype was determined by setting the Tachikawa number scale, λ_K, to 1. A vortex similar to 'Vane 5' setting but with a smaller core radius was used for the trajectory tests. For the 'Vane 5' setting (Table 2.1) with $V_{\theta_{max}} = 9.7\ \frac{m}{s}$ and full-scale vortex with $V_{\theta_{max}} = 97\ \frac{m}{s}$ representative of a full-scale EF5 tornado, the velocity scale, λ_V, was calculated as $\frac{1}{10}$. Table 2.3 shows the EF (Enhanced Fujita) scale and corresponding $V_{\theta_{max}}$ wind speeds.

Table 2.3 Enhanced Fujita scale

EF Scale	3-sec gust wind speed (m/s)
EF0	29-38
EF1	38-49
EF2	49-60
EF3	60-73
EF4	74-89
EF5	> 89

Based on the length scale (λ_L) chosen, the mass scale (λ_{mass}) was calculated from the Tachikawa number scaling in Equation 2.13, if acceleration due to gravity scale (λ_g) and air density scale (λ_ρ) are taken as 1.

$$\lambda_{mass} = {\lambda_L}^2 {\lambda_V}^2 \qquad \text{Equation 2.13}$$

The length scale (λ_L) of a wooden beam, 229 mm (9 in) in length and 76 mm (3 in) in diameter representing a 2x4 timber plank, can be taken as $\frac{1}{6}$ based on the smaller cylinder and the length scale of a light vehicle such as a car can be taken as $\frac{1}{80}$ based on the larger cylinder. The chosen length scales and calculated mass scales for the cylinder cases are shown in Table 2.4. It can be seen that the dimensions and density of the smaller cylinder in full-scale is similar to common construction grade 2x4 wood (300-500 $\frac{\text{kg}}{\text{m}^3}$) and the full-scale weight of the larger cylinder is similar in order of magnitude to a very light-weighted vehicle.

Table 2.4 Scaling parameters and prototype properties for models used in tornado simulator

	Model			Scaling Parameters		Prototype			
	Diameter (mm)	Length (mm)	Mass (g)	λ_L	λ_{mass}	Diameter (m)	Length (m)	Mass (kg)	Density (kg/m^3)
Sphere	25.4	-	0.19	-	-	-	-	-	-
	38.1	-	0.77	-	-	-	-	-	-
Cylinder	12.7	38.1	0.09	1/6	1/3,600	0.076	0.229	0.324	310
	25.4	76.2	0.60	1/80	1/640,000	2.032	6.096	384	19.42

It is important to note that the goal of this research was to be able to numerically predict the trajectory of a selected debris model in ISU's Tornado Simulator. The debris models were chosen based on ease-of-use in the simulator and can be adjusted in dimensions and weight in order to represent specific full-scale objects using Tachikawa scaling.

2.1.4 Experimental Setup

It has been found by past researchers (Tachikawa, 1983 and Kordi, 2011) that the initial conditions given to an object in vortex winds significantly affects the resulting trajectory. Therefore, objects were given multiple initial conditions in the form of initial height and radial position. Descriptions of various trajectory tests are given in Table 2.5. Cylinder tests were run multiple times for the same case in Tests 5 and 6.

Table 2.5 Debris trajectory test descriptions

	Test #	Object Diameter (mm)	Object Mass (g)	Radial distance from tornado center (mm) r_c = 530 mm	Initial Height (mm)
Sphere	1	25.4	0.19	305	279.5
	2	38.1	0.77	381	279.5
	3	25.4	0.19	381	152.5
	4	25.4	0.19	305	152.5
Cylinder	5	12.7	0.09	254	152.5
	6	25.4	0.60	254	152.5

The initial conditions for the spherical object in terms of radial distance, $r_o = r(t=0)$, and initial height, $h_o = h(t=0)$, are depicted in Figure 2.7 for a stationary vortex.

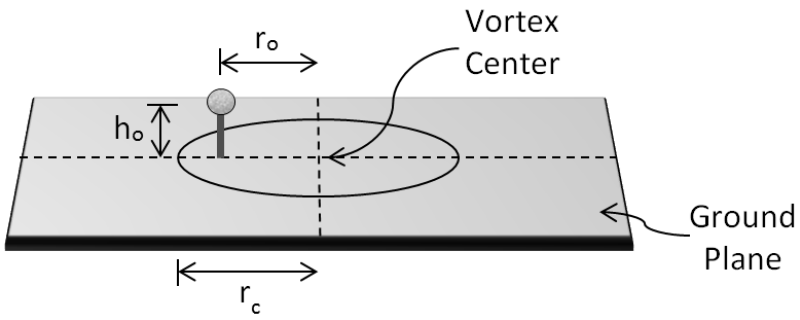

Figure 2.7 Sphere debris initial conditions

Using the length scale previously mentioned, it is clear that the initial heights are very high off the ground in a full-size tornado. The heights in this experiment were chosen in order to produce a long and easy to see trajectory. Ground effects of the tornado plane were neglected, so placing the object close to the ground would have introduced variability that was not accounted for in the study. In the future, more realistic initial conditions can be given to the debris objects and the resulting trajectories studied.

The object was held at given initial conditions in the vortex by a thin string held taut through a hollow pipe fixed to the ground plane as shown in Figure 2.8. Once the tornado simulator reached equilibrium for a given swirl ratio, the object was released by pulling the string through the object. The string was assumed to be small such that pulling it through the object created a negligible hole. The top end of the hollow pipe was taped so that there was no pressure difference on bottom of the object.

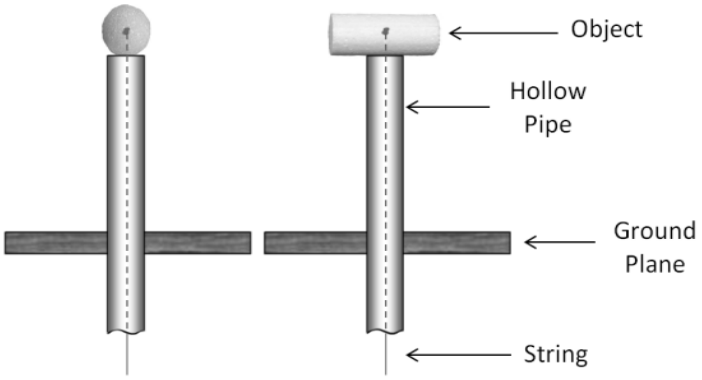

Figure 2.8 Initial placement of debris objects

The stereo-photogrammetry setup for these experiments was similar to the validation case. However, a larger grid was used because of the wide spread of the objects' trajectories. This was resolved by moving the grid and superimposing two grid pictures into one, as shown in Figure 2.9 and Figure 2.10.

Figure 2.9 Stereo-photogrammetry grid as seen in Camera 1 in the tornado simulator and in pixels

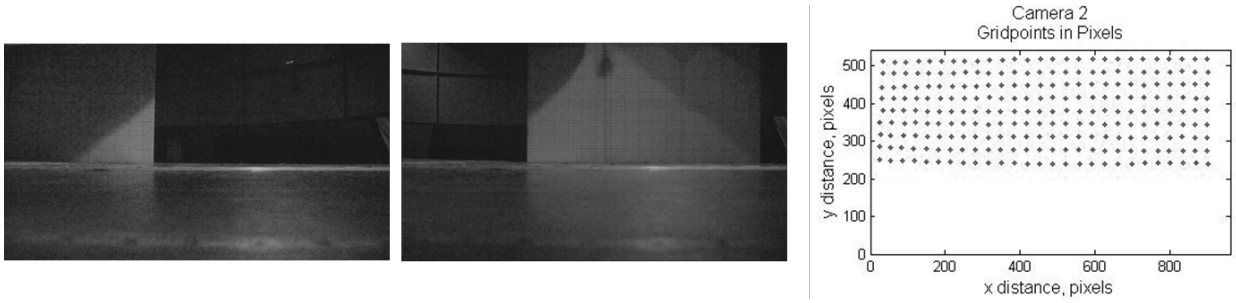

Figure 2.10 Stereo-photogrammetry grid as seen in Camera 2 in the tornado simulator and in pixels

One of the sphere trajectories (Test 2 from Table 2.5) is shown in Figure 2.11 and Figure 2.12 for each camera view, where the small dots are grid points and the open circles are the debris movement. The trajectory is recorded up to the point where the debris object first impacts the ground.

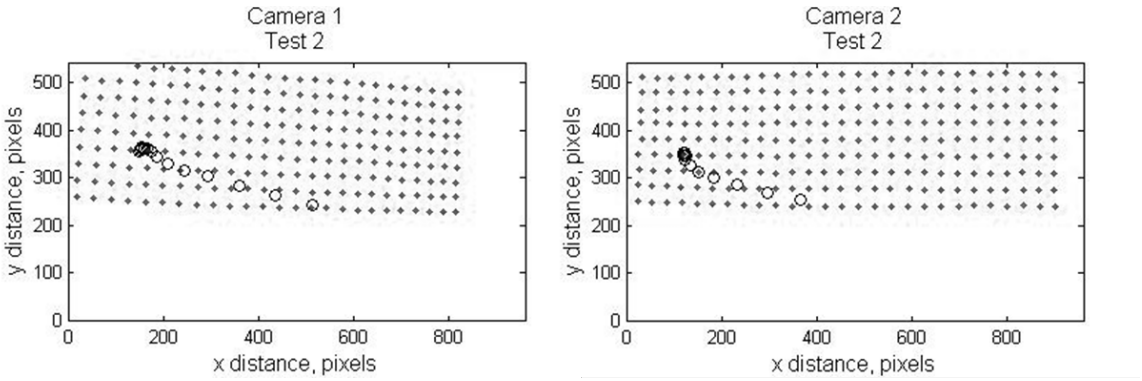

Figure 2.11 Trajectory for Test 2 in pixels as seen for Camera 1 (left) and Camera 2 (right)

The resulting trajectory for Test 2 is shown in Figure 2.12. The trajectories for the rest of the tests are shown in Appendix A.

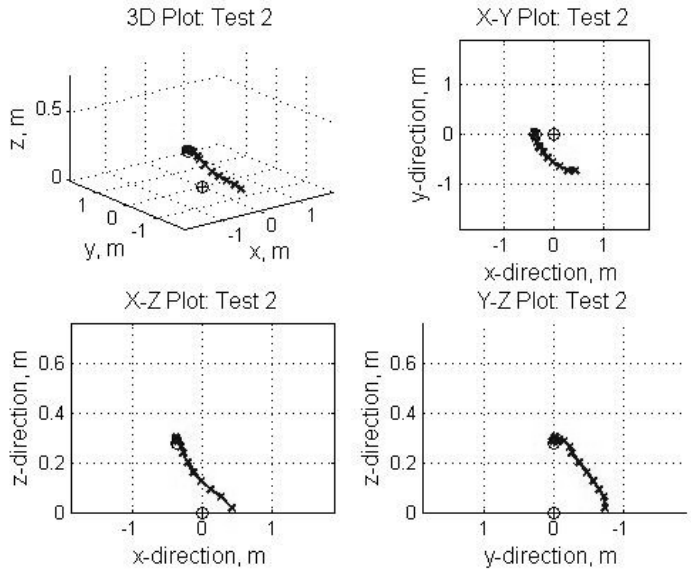

Figure 2.12 Stereo-photogrammetry trajectory, Test 2 (Table 2.5)

2.2 DEBRIS AERODYNAMIC COEFFICIENTS

For each of the debris objects described earlier, the aerodynamic force coefficients of the body needed to be determined before numerically predicting the trajectories.

2.2.1 Sphere Force Coefficients

The aerodynamic force coefficient of a sphere is well-known. In this study, it was assumed that the sphere was non-spinning and therefore there was only one aerodynamic drag coefficient, C_D, that was considered. The C_D is dependent on Reynolds number according to Figure 2.13.

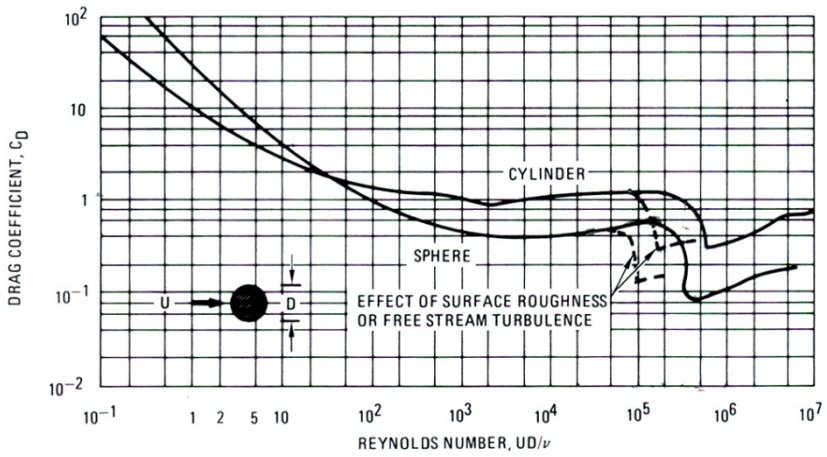

Figure 2.13 Coefficient of drag, C_D, for sphere versus Reynolds number (Blevins et. al., 1992)

The Reynolds number, Re, was calculated according to Equation 2.14.

$$Re = \frac{UD}{\nu} \qquad \text{Equation 2.14}$$

where ν is kinematic viscosity and is equal to $1.52 \times 10^{-5} \frac{m^2}{s}$ (at 21° C or 70° F and 1 atmo. pressure), U is the total velocity the sphere sees, and D is the diameter of the sphere. Throughout the debris trajectory, the total velocity changed enough to vary the Reynolds number of the two spheres used here within the range of approximately $2 \times 10^3 < Re < 1.1 \times 10^4$. The value of C_D remained relatively constant throughout this range, at approximately $C_D = 0.4$. However, in order to get a more accurate value of C_D, a digitizing program was used to digitize the data points from Figure 2.13 and is plotted in Figure 2.14.

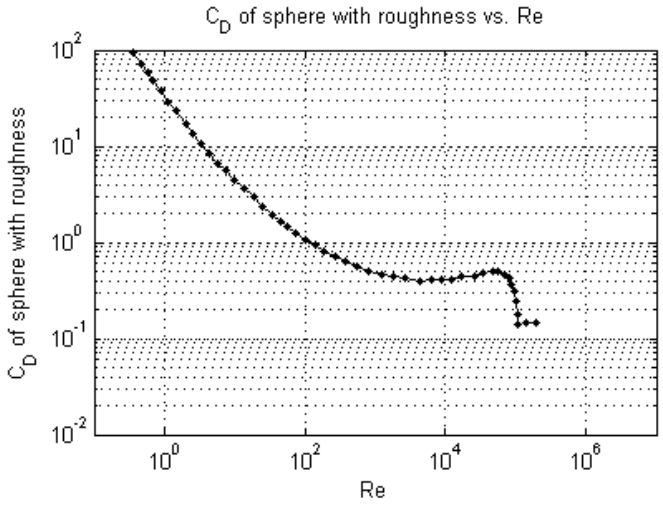

Figure 2.14 Digitized points of Coefficient of drag, C_D, for sphere versus Reynolds number

At each time step in the analytical solution, the value of C_D was obtained using interpolation based on the calculated Re of the flow around the sphere from Figure 2.14.

2.2.2 Cylinder Force And Moment Coefficients

A cylinder has three aerodynamic force coefficients and three aerodynamic moment coefficients about its principal axes as shown in Figure 2.15.

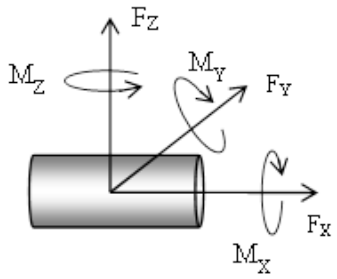

Figure 2.15 Aerodynamic force and moment coefficients on a circular cylinder

To determine the aerodynamic force and moment coefficients of a cylinder of aspect ratio (length:diameter) of 3:1, a cylinder of diameter D = 114 mm and length L = 343 mm was tested in the ISU Bill James Wind Tunnel (test section 3ft x 2.5ft) at Reynolds number of 3.75 to 6.5e04, similar to that of the tornado simulator. Force and moments were obtained using a JR3 force balance located below the wind tunnel floor plane at a distance (*h*) of 0.28 m from the center of the cylinder. These measurements were then used to calculate force and moment coefficients for the cylinder at various pitch and yaw angles. The test setup is shown in Figure 2.16.

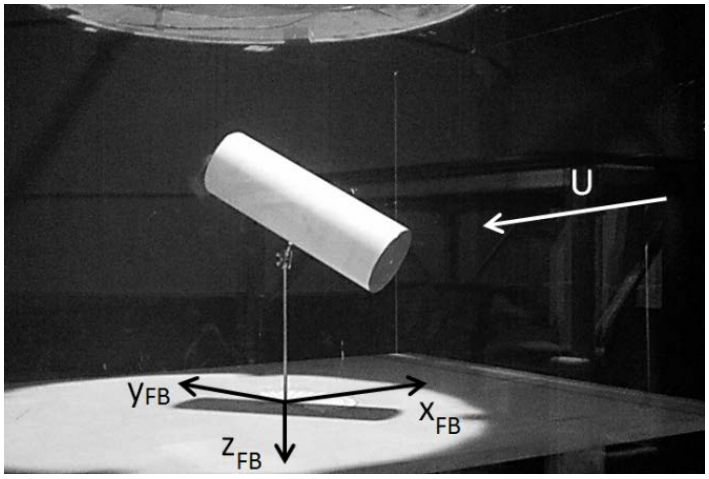

Figure 2.16 Experimental setup for measuring aerodynamic coefficients of circular cylinder

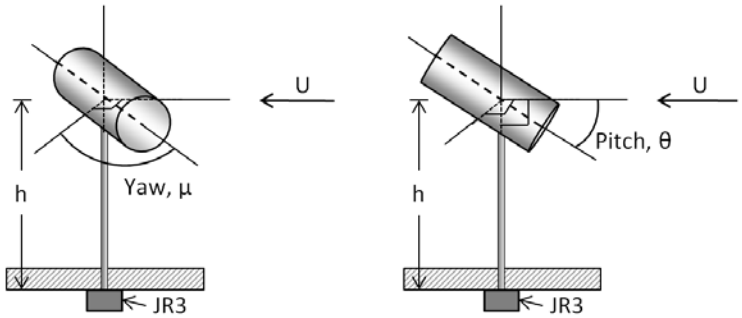

Figure 2.17 Depiction of yaw (μ) and pitch (θ) angles

Data was taken at two wind speeds, 5.0 m/s and 8.67 m/s, for combinations of 0°, 30°, 60°, 90° pitch (θ) and yaw (μ) angles as depicted in Figure 2.17. The Reynolds numbers corresponding to those speeds are 3.75e4 and 6.5e4, respectively. The measurements from the force balance were translated to the principal axes of the cylinder. Note that coordinates of the form x_{FB} are force balance centered coordinates. Coordinates of the form $x_{FB}{}^{*}$ are force-balance coordinates translated along the z-axis by a distance *h* to match the center of the cylinder (force-balance-translated coordinate system). Cylinder-based coordinates are all of the form x_p (principal coordinate system). Figure 2.18 - Figure 2.20 show the relationship between these coordinate systems.

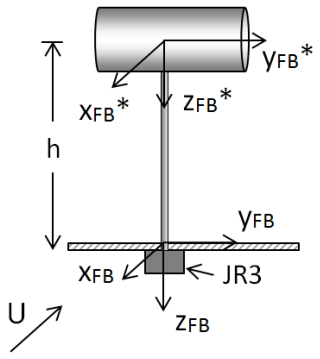

Figure 2.18 Force-balance and force-balance-translated coordinate systems

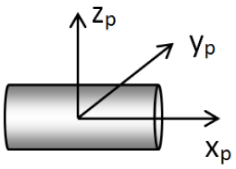

Figure 2.19 Principle coordinate system

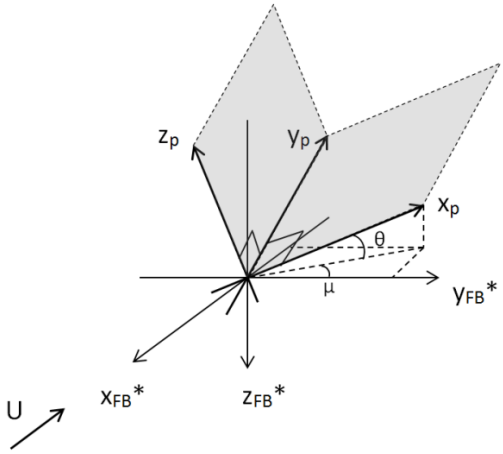

Figure 2.20 Relationship between force-balance-translated and principle coordinate systems

The coordinate transformation matrix for the forces were calculated using Euler angles. Euler proved that the general motion of a rigid body when one point is held fixed corresponds to a series of three rotations about three orthogonal coordinate axes. These three rotations are commonly called yaw, pitch, and roll. In this case, roll is zero (rotation about x_p) so that transformation corresponding to roll was neglected. Yaw is the positive rotation about the z^*-axis (μ) and pitch is the negative rotation about the resultant y'-axis (θ), as shown in Figure 2.21 and Figure 2.22.

$\boldsymbol{X'} = \boldsymbol{R}_{z^*}\boldsymbol{X}^*$, where $\boldsymbol{X}^*$ is vector of original coordinates and $\boldsymbol{X'}$ is vector of transformed coordinates and $\boldsymbol{R}_{z^*}$ is coordinate transformation matrix for rotation (μ) about 'z^*' axis, shown in Figure 2.21 and Equation 2.15.

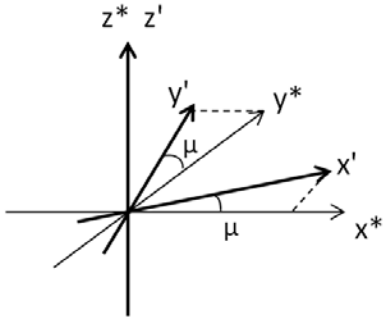

Figure 2.21 Yaw rotation (μ) about '$\boldsymbol{z}^*$' axis.

$$\boldsymbol{R}_{z^*}(\mu) = \begin{bmatrix} \cos\mu & -\sin\mu & 0 \\ \sin\mu & \cos\mu & 0 \\ 0 & 0 & 1 \end{bmatrix} \qquad \text{Equation 2.15}$$

$\boldsymbol{X}'' = \boldsymbol{R}_{y'}\boldsymbol{X}'$, where $\boldsymbol{X}'$ is vector of original coordinates and $\boldsymbol{X}''$ is vector of transformed coordinates and $\boldsymbol{R}_{y'}$ is coordinate transformation matrix for rotation (θ) about 'y'' axis, shown in Figure 2.22 and Equation 2.16.

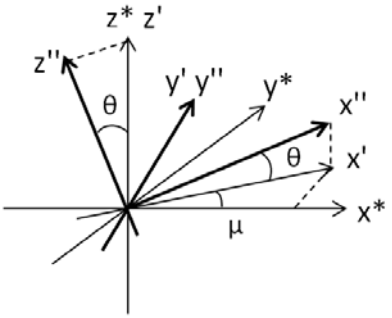

Figure 2.22 Pitch rotation (θ) about '$\boldsymbol{y}'$' axis.

$$\boldsymbol{R}_{y'}(\theta) = \begin{bmatrix} \cos\theta & 0 & -\sin\theta \\ 0 & 1 & 0 \\ \sin\theta & 0 & \cos\theta \end{bmatrix} \qquad \text{Equation 2.16}$$

The resultant transformation matrix is formed by multiplying the two matrices together in the order the rotations are performed (first yaw, then pitch), shown in Equation 2.17.

$$\boldsymbol{R}_{y'z^*}(\mu,\theta) = \boldsymbol{R}_{y'}(\theta)\boldsymbol{R}_{z^*}(\mu) = \begin{bmatrix} \cos\mu\cos\theta & -\cos\theta\sin\mu & -\sin\theta \\ \sin\mu & \cos\mu & 0 \\ \cos\mu\sin\theta & -\sin\mu\sin\theta & \cos\theta \end{bmatrix} \quad \text{Equation 2.17}$$

Thus,

$$\begin{Bmatrix} x'' \\ y'' \\ z'' \end{Bmatrix} = \begin{Bmatrix} x_p \\ y_p \\ z_p \end{Bmatrix} = \boldsymbol{R}_{y'z^*} \begin{Bmatrix} x^* \\ y^* \\ z^* \end{Bmatrix} \quad \text{Equation 2.18}$$

The determinant of the transformation matrix in Equation 2.18 is 1, which shows that the transformation is orthogonal. However, the input coordinates $\begin{Bmatrix} x^* \\ y^* \\ z^* \end{Bmatrix}$ are not the force-balance-translated coordinates $\begin{Bmatrix} {x_{FB}}^* \\ {y_{FB}}^* \\ {z_{FB}}^* \end{Bmatrix}$ shown in Figure 2.18. In this case the relationship between these two coordinate systems is given by Equation 2.19.

$$\begin{Bmatrix} {x_{FB}}^* \\ {y_{FB}}^* \\ {z_{FB}}^* \end{Bmatrix} = \begin{Bmatrix} -y^* \\ x^* \\ -z^* \end{Bmatrix} \quad \text{Equation 2.19}$$

Now the final transformation matrix from force-balance coordinates to cylinder centered coordinates is given by Equation 2.20 and the transformation equation is Equation 2.21.

$$\boldsymbol{R} = \begin{bmatrix} -R_{12} & R_{11} & -R_{13} \\ -R_{22} & R_{21} & -R_{23} \\ -R_{32} & R_{31} & -R_{33} \end{bmatrix} = \begin{bmatrix} \cos\theta\sin\mu & \cos\mu\cos\theta & \sin\theta \\ -\cos\mu & \sin\mu & 0 \\ \sin\mu\sin\theta & \cos\mu\sin\theta & -\cos\theta \end{bmatrix} \quad \text{Equation 2.20}$$

$$\begin{Bmatrix} x_P \\ y_P \\ z_P \end{Bmatrix} = \boldsymbol{R} \begin{Bmatrix} x_{FB} \\ y_{FB} \\ z_{FB} \end{Bmatrix} \quad \text{Equation 2.21}$$

The determinant of $\boldsymbol{R} = -1$ which verifies that the transformation is orthogonal. The transformation of the *forces* from the force-balance centered coordinate system to the principal axis of the cylinder-centered coordinate system is shown in Equation 2.22.

$$\begin{Bmatrix} F_{x_P} \\ F_{y_P} \\ F_{z_P} \end{Bmatrix} = \boldsymbol{R} \begin{Bmatrix} F_{x_{FB}} \\ F_{y_{FB}} \\ F_{z_{FB}} \end{Bmatrix} \quad \text{Equation 2.22}$$

The cylinder-based coordinate system of the moments is found by the relationships in Equation 2.23 - Equation 2.25.

$$M_{y_{FB}}{}^{*} = -F_{x_{FB}} h + M_{y_{FB}} \quad \text{Equation 2.23}$$

$$M_{x_{FB}}{}^{*} = F_{y_{FB}} h + M_{x_{FB}} \quad \text{Equation 2.24}$$

$$M_{z_{FB}}{}^{*} = M_{z_{FB}} \quad \text{Equation 2.25}$$

These equations are put into matrix form in Equation 2.26 and Equation 2.27.

$$\begin{Bmatrix} M_{x_P} \\ M_{y_P} \\ M_{z_P} \end{Bmatrix} = \boldsymbol{R} \begin{Bmatrix} M_{x_{FB}}{}^{*} \\ M_{y_{FB}}{}^{*} \\ M_{z_{FB}}{}^{*} \end{Bmatrix} = \boldsymbol{R} \begin{Bmatrix} M_{x_{FB}} \\ M_{y_{FB}} \\ M_{z_{FB}} \end{Bmatrix} + \boldsymbol{R} \begin{Bmatrix} hF_{y_{FB}} \\ -hF_{x_{FB}} \\ 1 \end{Bmatrix} \quad \text{Equation 2.26}$$

$$\begin{Bmatrix} M_{x_P} \\ M_{y_P} \\ M_{z_P} \end{Bmatrix} = \boldsymbol{R} \begin{Bmatrix} M_{x_{FB}} \\ M_{y_{FB}} \\ M_{z_{FB}} \end{Bmatrix} + h\boldsymbol{R} \begin{bmatrix} 0 & 1 & 0 \\ -1 & 0 & 0 \\ 0 & 0 & 0 \end{bmatrix} \begin{Bmatrix} F_{x_{FB}} \\ F_{y_{FB}} \\ F_{z_{FB}} \end{Bmatrix} \quad \text{Equation 2.27}$$

Let

$$\boldsymbol{T} = \begin{bmatrix} 0 & 1 & 0 \\ -1 & 0 & 0 \\ 0 & 0 & 0 \end{bmatrix} \quad \text{Equation 2.28}$$

The transformation of the *moments* from the force-balance centered coordinate system to the principal axis of the cylinder-centered coordinate system takes the final form in Equation 2.29.

$$\begin{Bmatrix} M_{x_P} \\ M_{y_P} \\ M_{z_P} \end{Bmatrix} = \boldsymbol{R} \begin{Bmatrix} M_{x_{FB}} \\ M_{y_{FB}} \\ M_{z_{FB}} \end{Bmatrix} + \mathrm{h}\, \boldsymbol{R}\, \boldsymbol{T} \begin{Bmatrix} F_{x_{FB}} \\ F_{y_{FB}} \\ F_{z_{FB}} \end{Bmatrix} \quad \text{Equation 2.29}$$

The projected area (A_p) for each combination of yaw and pitch angles was found using Equation 2.30 and Equation 2.31, where 'D' and 'L' correspond to the diameter and length of the cylinder, respectively. In Equation 2.31, μ^* is the angle between the vertical plane normal to wind speed and the vertical plane containing the axis of the cylinder.

$$A_p = DL\cos(\mu^*) + \pi\frac{D^2}{4}\sin(\mu^*) \quad \text{Equation 2.30}$$

$$\mu^* = \sin^{-1}[\sin(\mu)\cos(\theta)] \quad \text{Equation 2.31}$$

Force and moment coefficients are dependent on pitch and yaw angles. The forces and moments were normalized with dynamic pressure $(\frac{1}{2}\rho U^2)$ and projected area (A_p) to give the resulting force and moment coefficients. Equation 2.32 and Equation 2.33 show the normalization for the *x*-component of force and moment. The other coefficients were calculated similarly.

$$C_{F_x} = \frac{F_{x,p}}{\frac{1}{2}\rho U^2 A_p} \quad \text{Equation 2.32}$$

$$C_{M_x} = \frac{M_{x,p}}{\frac{1}{2}\rho U^2 A_p D} \quad \text{Equation 2.33}$$

The average force and moment coefficients from the wind tunnel tests for two different velocities can be found in Appendix B. Equation 2.34 gives the force and moment coefficients for pitch (θ) and yaw (μ) angles both equal to zero.

$$\begin{Bmatrix} C_{F_x} \\ C_{F_y} \\ C_{F_z} \end{Bmatrix} = \begin{Bmatrix} 0.04 \\ 1.01 \\ -0.21 \end{Bmatrix}, \qquad \begin{Bmatrix} C_{M_x} \\ C_{M_y} \\ C_{M_z} \end{Bmatrix} = \begin{Bmatrix} -0.56 \\ 0.08 \\ 0.06 \end{Bmatrix} \quad \text{Equation 2.34}$$

CHAPTER 3. NUMERICAL METHODOLOGY

3.1 PREDICTION OF TORNADIC WIND VELOCITY TIME HISTORIES

In order to obtain the aerodynamic forces acting on the debris in ISU's Tornado Simulator, it was necessary to know the tornadic wind velocity experienced at the specific location of the debris object. The tornado was simulated on a smooth ground plane representing open terrain conditions (Haan et al., 2010). A setting similar to 'Vane 5' setting (Haan et al., 2008) given in Table 2.1 was used for this study. The 'Vane 5' setting refers to a specific 'vane angle' setting in the tornado simulator to generate a tornado vortex of a specific vortex structure (r_c = 0.53 m), velocity ($V_{\theta,max}$ = 9.7 m/s) and swirl ratio (S=1.14). The difference between the setting used for this study and the 'Vane 5' setting given in Table 2.1 was the core radius, r_c. The radius of the core was found experimentally as the radius at which V_θ was maximum at a height of 31.8 mm (1.5 inch) from the ground plane, shown in Figure 3.1.

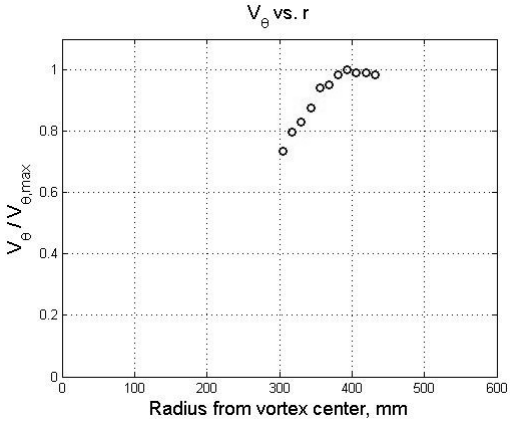

Figure 3.1 Normalized V_θ measurements to determine core radius r_c of 'Vane 5' setting (Haan et al., 2008) at z = 31.8 mm height

Therefore, in this study an r_c = 0.40 m was used. Using Equation 2.11, this value of core radius gives a swirl ratio of S = 0.65. Tachikawa scaling was used to scale the tornado and debris objects, as mentioned in section 2.1.3.

A computer program was written to use the time/spatial histories of radial and tangential velocity, V_r and V_θ, calculated from Thampi et al., 2010 for the 'Vane 5' setting. This program was used for the current study because the vortex structure of the tornado used in the trajectory experiments was very similar to the 'Vane 5' setting tornado. For the purposes of this research, the tornado is non-translating and velocity vectors were calculated at each time step based the position coordinates of the object.

The methodology used in Thampi et al., 2010 as described on the following pages can be adopted to simulate tornadoes of other swirl ratios and vortex structures. Figure 3.2 shows the normalized tangential velocity ($V_\theta/V_{\theta,max}$) as a function of r/r_c at various heights,

where r is the radial distance from the center of the vortex and r_c is the radius of the vortex core.

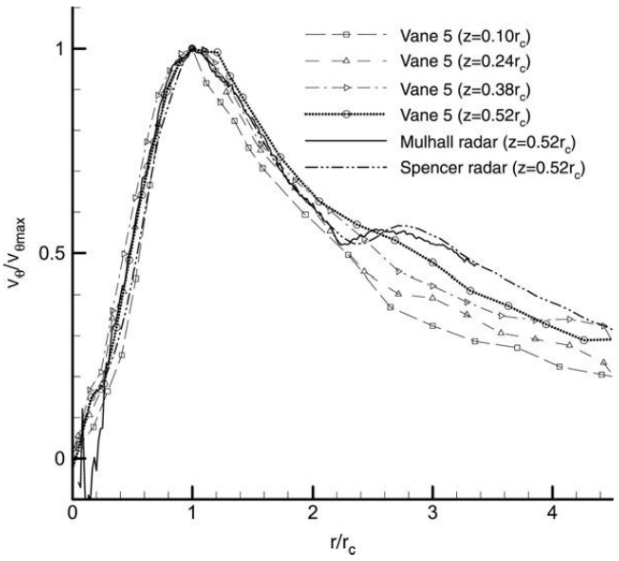

Figure 3.2 Normalized V_θ profile for 'Vane 5' setting (Haan et al., 2008)

The current research used the non-dimensional curve in Figure 3.2 with height $z = 0.52r_c$. It was assumed that this curve was constant with height in the tornado, for locations not too close to the ground. In order to model this curve, it was split into three ranges of r: (1) from the center of the vortex to r_c, (2) the flat region from r_c to $1.224r_c$ and (3) $r \geq 1.224r_c$. The equations fit to each of these ranges are shown below in Equation 3.1 - Equation 3.3.

$$V_\theta = \frac{r}{r_c} V_{\theta,max}\,, \quad 0 < r < r_c \qquad \text{Equation 3.1}$$

$$V_\theta = V_{\theta,max}\,, \quad r_c < r < 1.224r_c \qquad \text{Equation 3.2}$$

$$V_\theta = 1.2\left(\frac{r}{r_c}\right)^{-0.9} V_{\theta,max}\,, \quad r > 1.224r_c \qquad \text{Equation 3.3}$$

Curve fitting was repeated to find equations for the radial velocity. The normalized radial velocity profiles ($V_r/V_{\theta,max}$) at four radial distances $1r_c$, $2r_c$, $3r_c$, $4r_c$ as a function of non-dimensional height z/r_c corresponding to 'Vane 5' setting (Haan et al., 2008) were chosen

and are shown in Figure 3.3. Four curves were fit to these profiles and are given by Equation 3.4. The constants C_1, C_2, and n in Equation 3.4 as listed in Table 3.1 correspond to the four different radial velocity profiles and $V_{\theta,max}(r)$ is the maximum tangential velocity at a radial distance r.

$$V_r = C_1 \left(\frac{z}{r_c}\right)^n \left[1 - erf\left(C_2 \frac{z}{r_c}\right)\right] V_{\theta,max}(r) \qquad \text{Equation 3.4}$$

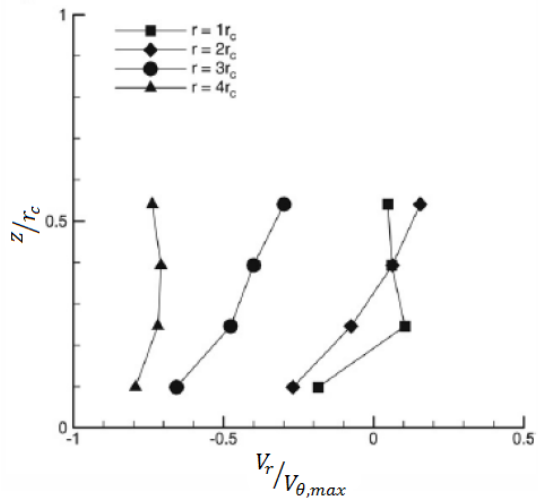

Figure 3.3 Normalized V_r profiles at four radial distances for 'Vane 5' setting (Haan et al., 2008)

Table 3.1 Constants for different radial velocity curves

r/r_c	C_1	C_2	n
1	18.84	2.28	3.21
2	-2.35	3.74	1.00
3	-2.40	3.16	0.69
4	-0.40	0.17	0.02

The calculation of vertical velocity was neglected in the study done by Thampi et al. 2010. The vertical component of the wind velocity, V_z, was included in the current procedure based

on a linear interpolation of data obtained for the 'Vane 5' setting in ISU's Tornado Simulator. Vertical velocity varies with both radius and height as shown in Figure 3.4.

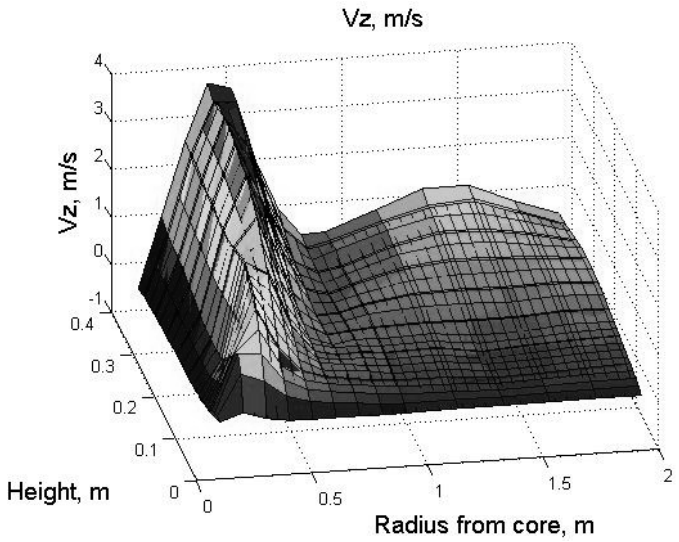

Figure 3.4 V_z data taken at various height, *z*, and radius, *r*, locations

A computer program was written to compute the time and spatial histories of V_r, V_θ, and V_z at the center of the debris object for a stationary tornado as shown in Figure 3.5.

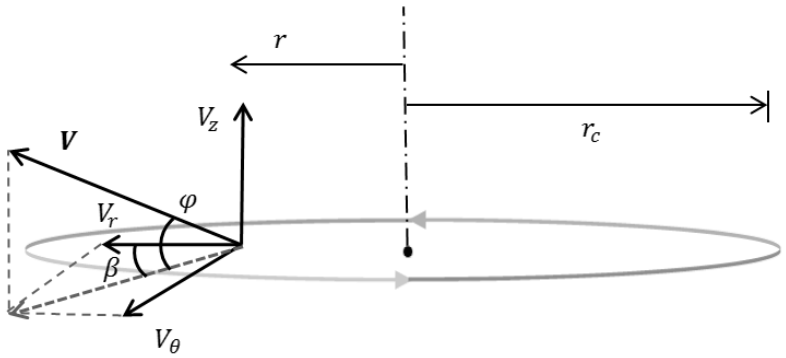

Figure 3.5 Tornadic wind velocity components and corresponding angles

The inputs required for this program are $V_{\theta,max}$, r_c, and the (x, y, z) coordinates of the center of the object. The velocity components are calculated for the location of the object and the output of the program is (V_r, V_θ, V_z) data at that position.

3.2 TRAJECTORY PROPAGATION METHODOLOGY

3.2.1 Introduction

Previous research on debris movement in 3D vortex winds has built the equations of motion around many assumptions, which in turn has limited the number of forces acting on the object during the trajectory. The goal of this project was to take into account all reasonable forces acting on the object. In Maruyama's simulation of wind-borne debris particles in tornadic winds (et al. 2011), the only force considered was aerodynamic drag acting on the object. Kordi et al. (2009) argued that the buoyancy parameter is important to consider when looking at plate debris in uniform flow. In this study, it is believe that force due to static pressure in the tornado vortex is also an important force to consider. For this reason buoyancy, force due to centripetal acceleration, and pressure forces are included in the equations of motion for both the sphere and circular cylinder debris.

The numerical integration was carried out to calculate the velocity vector $\overline{\boldsymbol{V}}$ of the flying debris object using a constant acceleration method with the small time step $\Delta t = 0.0035$ sec (as used in Thampi, 2010), shown in Equation 3.5 and Equation 3.6.

$$\overline{\boldsymbol{V}}_{i+1} = \overline{\boldsymbol{V}}_i + \boldsymbol{A}_i \Delta t \qquad \text{Equation 3.5}$$

$$\boldsymbol{X}_{i+1} = \boldsymbol{X}_i + \overline{\boldsymbol{V}}_i \Delta t + \frac{\boldsymbol{A}_i}{2} \Delta t^{\,2} \qquad \text{Equation 3.6}$$

3.2.2 Sphere

3.2.2.1 Overview of Forces

A sphere is the simplest aerodynamic body to consider in trajectory motion because of its symmetrical shape. Assuming a non-rotating sphere, the only aerodynamic force to consider (besides the three mentioned above) is drag. Figure 3.6 shows the forces acting on a sphere in three-dimensional tornadic flow.

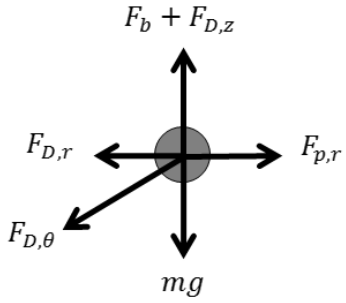

Figure 3.6 Forces acting on sphere in three-dimensional flow

Based on Newton's second law, Equation 3.7 - Equation 3.9 describe the motion of a (non-rotating) spherical object.

$$ma_r = m\left(\frac{d^2r}{dt^2} - \frac{V_\theta^2}{r}\right) = F_{D,r} - F_{p,r} \qquad \text{Equation 3.7}$$

$$ma_\theta = m\frac{d^2\theta}{dt^2} = F_{D,\theta} \qquad \text{Equation 3.8}$$

$$ma_z = m\frac{d^2z}{dt^2} = F_{D,z} + F_b - mg \qquad \text{Equation 3.9}$$

where

$F_D = \frac{1}{2}\rho|U|^2 C_D \pi \frac{D^2}{4}$ = Total Aerodynamic Drag Force Equation 3.10

$F_{D,r} = F_D \cos\varphi \cos\beta$ = Radial Component of F_D Equation 3.11

$F_{D,\theta} = F_D \cos\varphi \sin\beta$ = Tangential Component of F_D Equation 3.12

$F_{D,z} = F_D \sin\varphi$ = Vertical Component of F_D Equation 3.13

$F_{p,r} = \int P(r)$ = Static Pressure-Induced Force in Radial Direction Equation 3.14

$F_b = \rho g \frac{1}{6}\pi D^3$ = Buoyancy Force Equation 3.15

Equation 3.14 is expanded into Equation 3.21. The total velocity, $\boldsymbol{U} = \sqrt{U_r^2 + U_\theta^2 + U_z^2}$, was calculated as the resultant velocity of the tornadic wind, $\boldsymbol{V}$, minus the velocity of the debris object, $\overline{\boldsymbol{V}}$, shown in Equation 3.16.

$$\boldsymbol{U} = \boldsymbol{V} - \overline{\boldsymbol{V}} \quad \text{Equation 3.16}$$

The static pressure, $P(r)$, at each radial location, r, in the vortex was assumed constant with height, so the average static pressure is shown in Figure 3.7 vs. radius from vortex center. A third-order polynomial line was curve fitted to the measurement data.

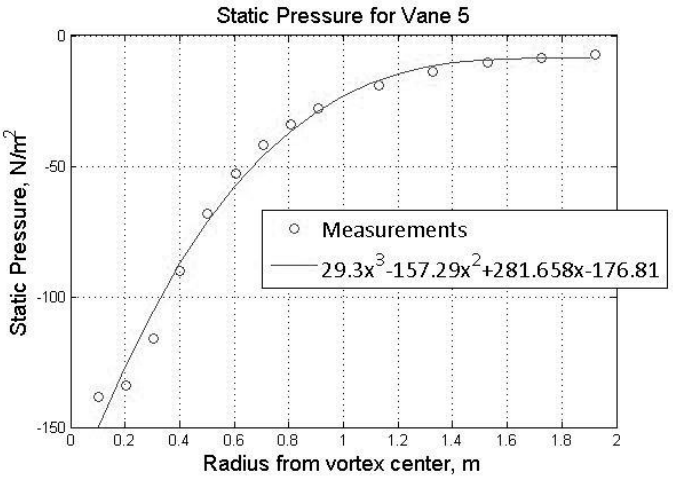

Figure 3.7 Static pressure measurements as function of radius from vortex center for 'Vane 5' setting

The incremental pressure force in the radial direction, $dF_{p,r}$, acting on a small section of the sphere (Figure 3.8) at any instant due to static pressure is shown in Equation 3.17 and Equation 3.18, where R is the radius of the sphere. Angles used in this equation are shown in Figure 3.8.

$$dF_{p,r} = P(r)R^2 d\theta d\varphi \cos(\theta)\cos(\varphi) \qquad \text{Equation 3.17}$$

$$P(r) = 29.3r^3 - 157.29r^2 + 281.658r - 176.81 \qquad \text{Equation 3.18}$$

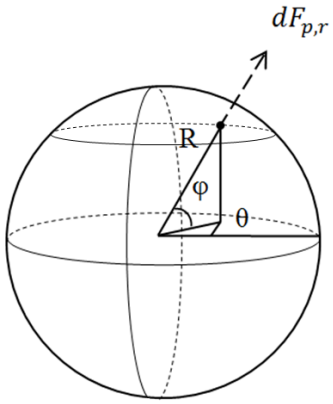

Figure 3.8 Incremental pressure force, $dF_{p,r}$, acting on a small section of the sphere

Let r_1 be the distance from the center of the vortex to the closest edge of the sphere along the radial direction of the vortex. Then the distance from the center of the sphere to the center of the vortex is $r = r_1 + R$. Using the angles shown in Figure 3.8, the distance from the center of the vortex to any point on the sphere is given by Equation 3.19.

$$r = r_1 + R - R\cos(\theta)\cos(\varphi) \qquad \text{Equation 3.19}$$

The total pressure force acting on the sphere in the radial direction towards the center of the vortex, $F_{p,r}$, was found by integrating the incremental pressure force over the surface area of the sphere. The surface area of a sphere was found by integrating Equation 3.20.

$$A_{surf} = \int_{0=\theta}^{2\pi} \int_{0=\varphi}^{\pi} \sin(\varphi)\, d\varphi d\theta \qquad \text{Equation 3.20}$$

Thus, $F_{p,r}$ was calculated in Equation 3.21 by combining Equation 3.17 and Equation 3.20.

$$F_{p,r} = \int_{0=\theta}^{2\pi} \int_{0=\varphi}^{\pi} P(r) R^2 \cos(\theta) \cos(\varphi) \sin(\varphi)\, d\varphi d\theta \qquad \text{Equation 3.21}$$

The value of $P(r)$ closer to the center of the vortex will always be more negative than the value farther away, so the pressure force on the sphere will always pull the sphere towards the center of the vortex.

3.2.2.2 Validation of Sphere Forces

The experimental procedure used to validate the stereo-photogrammetry setup described in section 2.1.2 was used to validate the equations for forces acting on the debris objects in the tornado simulator. An object was hung from the center of the tornado simulator and when the tornado simulator was turned on, the object reached an equilibrium spinning at a certain *r* and *h* depending on the object properties, length *l* of string, and the swirl ratio of the vortex. The height *h* was measured manually inside the simulator, and the radius *r* was calculated from that. The goal in this validation test was to accurately calculate the height and radius at which an object will reach equilibrium for various swirl ratios. The same low swirl ratios were used for these tests (0.08-0.24) as for the stereo-photogrammetry validation tests. However it is believed that the forces equations can be used in any swirl ratio.

Two spheres were used in this experiment of different diameters and masses. The spheres were of diameter 0.0254m (1.0 inch) and 0.0508m (2.0 inches) and masses 2.6e-4 kg and 3.55e-2 kg, respectively. The forces acting on the sphere when tied to a string are shown in Figure 3.9.

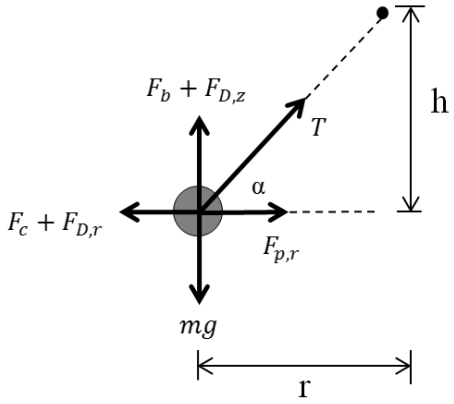

Figure 3.9 Forces acting on a sphere in the validation test

The forces were calculated as shown in Equation 3.10 - Equation 3.15, where coefficient of drag, C_D, was calculated using an interpolation of Figure 2.14. Equation 3.21 was used to find the force due to static pressure, $F_{p,r}$, however Equation 3.18 was modified to fit the static pressure measurements taken for the appropriate vortex structure. The acceleration component, $\frac{d^2r}{dt^2}$, in the radial direction and a_z in the vertical direction were set to zero, shown in Equation 3.22 and Equation 3.24, and substituted into Equation 3.7 and Equation 3.9. The equilibrium equations are shown in Equation 3.23 and Equation 3.25, where T is the tension force in the string.

$$\frac{d^2r}{dt^2} = 0 \qquad \text{Equation 3.22}$$

$$T\cos\alpha = F_c + F_{D,r} - F_{p,r} \quad \text{Equation 3.23}$$

$$\frac{d^2z}{dt^2} = 0 \quad \text{Equation 3.24}$$

$$T\sin\alpha = mg - F_b - F_{D,z} \quad \text{Equation 3.25}$$

where

$$F_c = m\frac{V_\theta^2}{r} \quad \text{Equation 3.26}$$

Equation 3.26 gives centrifugal force, where *r* is the radius of curvature and is equal to the radial position of the center of the sphere to the center of the vortex. Equation 3.23 and Equation 3.25 were combined by solving for T. The resulting equation is shown in Equation 3.27.

$$\left(F_c - F_{D,r} - F_{p,r}\right)\tan\alpha + F_b + F_{D,z} - mg = 0 \quad \text{Equation 3.27}$$

Angle α is directly related to *h* and *r* by Equation 3.28.

$$tan\,\alpha = {}^{h}/_{r} \quad \text{Equation 3.28}$$

Therefore, Equation 3.26 and Equation 3.28 were substituted into Equation 3.27 to give Equation 3.29, which was solved for *r*.

$$r^2\left[F_b + F_{D,z} - mg\right] + r\left[h\left(F_{D,r} - F_{p,r}\right)\right] + hmV_\theta^2 = 0 \quad \text{Equation 3.29}$$

This final equation is quadratic for *r*, however it includes *h* and all the forces are functions of *r* and *h*. For this reason, the equation must be solved iteratively. The resulting calculated *r* for each sphere and various swirl ratios and fan speeds were compared with actual measured *r* in Table 3.2. Plots of velocity and pressure measurements for the various swirl ratios and fan speeds can be found in Appendix C.

Table 3.2 Results of the sphere forces validation test

Sphere Diameter (mm)	Mass (g)	Swirl Ratio	$V_{\theta,max}$ (m/s)	*h* (mm)	*l* (mm)	Actual *r* (mm)	Calculated *r* (mm)	%diff
25.4	0.26	0.08	2.04	749	889	478	460	3.80
			1.97	483	635	413	430	4.31
			2.49	737	927	563	542	3.70
		0.24	1.89	749	978	628	586	6.80
			2.22	737	1003	667	618	7.43
50.8	35.5	0.08	3.07	737	914	542	578	6.72
		0.24	2.66	724	940	599	628	4.76
			3.10	724	1016	713	699	1.97

The percent difference between calculated *r* and the actual measured *r* value is less than 10% for all cases. This experimental error is considered acceptable and shows that the forces used in calculations adequately model the forces acting on the sphere.

3.2.3 Circular Cylinder

3.2.3.1 Overview of Forces And Moments

A cylinder has three aerodynamic force coefficients and three aerodynamic moment coefficients about its principal axes as shown in Figure 2.15. Wind tunnel tests were performed on a cylinder of aspect ratio of 3:1 (length to diameter) as described in section 2.2.2 to experimentally determine these force and moment coefficients for different cylinder orientations with respect to the wind velocity vector. Figure 3.10 shows the orientation of the cylinder-based principle coordinate system of the form '$\boldsymbol{X}_p$' with respect to the global coordinate system. The pitch and yaw angles between the principle and global coordinate

system include a subscript '$_G$'. These angles are different than the true pitch (θ) and yaw (μ) angles made with respect to the total velocity vector, which correspond to the force and moment data collected in the wind tunnel tests, as shown in Figure 2.20.

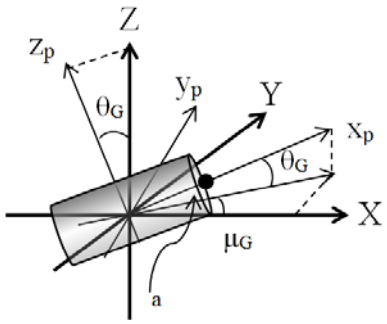

Figure 3.10 Relationship between principle and global coordinate systems

The total wind velocity the object experiences in the flow-field, $\boldsymbol{U} = \sqrt{U_x^2 + U_y^2 + U_z^2}$, was calculated as the velocity of the tornadic wind, $\boldsymbol{V}$, minus the velocity of the debris object, $\overline{\boldsymbol{V}}$ as shown in Equation 3.16. Figure 3.11 shows the orientation and angles in the global coordinate system of the total velocity vector.

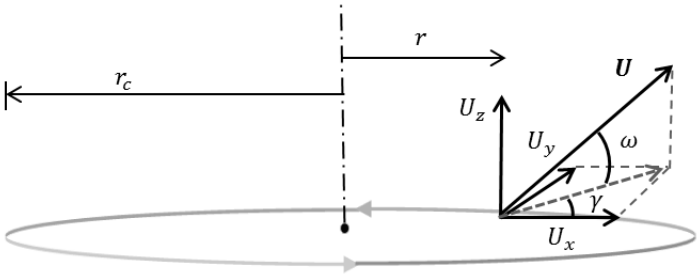

Figure 3.11 Total velocity components and corresponding angles in global coordinate system

In order to determine the force and moment coefficients obtained from the wind tunnel tests, the true pitch (θ) and yaw (μ) made with respect to the total velocity vector, U, was determined first. This required a series of coordinate transformations using the same

principles as described in section 2.2.2. First, the coordinates of point 'a', (x_a, y_a, z_a) on the cylinder shown in Figure 3.10 were determined in the global coordinates. At each time step the pitch (θ_G) and yaw (μ_G) angles between the principle and global coordinate system were known. Therefore, the transformation was done via Equation 2.17 where θ_G and μ_G were substituted for θ and μ, respectively, as shown in Equation 3.30 and Equation 3.31.

$$\boldsymbol{R}_{y'z^*}(\mu_G, \theta_G) = \boldsymbol{R}_{y'}(\theta_G)\boldsymbol{R}_{z^*}(\mu_G)$$

$$= \begin{bmatrix} \cos\mu_G \cos\theta_G & -\cos\theta_G \sin\mu_G & -\sin\theta_G \\ \sin\mu_G & \cos\mu_G & 0 \\ \cos\mu_G \sin\theta_G & -\sin\mu_G \sin\theta_G & \cos\theta_G \end{bmatrix} \quad \text{Equation 3.30}$$

Let l be the length of the cylinder. Thus,

$$\begin{Bmatrix} x_a \\ y_a \\ z_a \end{Bmatrix} = \boldsymbol{R}_{y'z^*}(\mu_G, \theta_G) \begin{Bmatrix} l/2 \\ 0 \\ 0 \end{Bmatrix} \quad \text{Equation 3.31}$$

Therefore, the coordinates of point 'a' and the total velocity vectors were all known in the global coordinate system. The coordinates of point 'a' $(x_{a,U}, y_{a,U}, z_{a,U})$ with respect to the direction of the magnitude of the total velocity vector, U, was found next in order to determine the true pitch (θ) and yaw (μ) angles. This was done via the inverse of Equation 2.17 where ω and $\tau = -(\pi/2 - \gamma)$ from Figure 3.11 were substituted for θ and μ, respectively, as shown in Equation 3.32 and Equation 3.33.

$$\boldsymbol{R}_{y'z^*}(\tau, \omega) = \boldsymbol{R}_{y'}(\omega)\boldsymbol{R}_{z^*}(\tau) = \begin{bmatrix} \cos\tau \cos\omega & -\cos\omega \sin\tau & -\sin\omega \\ \sin\tau & \cos\tau & 0 \\ \cos\tau \sin\omega & -\sin\tau \sin\theta_G & \cos\omega \end{bmatrix} \quad \text{Equation 3.32}$$

Thus,

$$\begin{Bmatrix} x_{a,U} \\ y_{a,U} \\ z_{a,U} \end{Bmatrix} = \boldsymbol{R}_{y'z^*}{}^{-1}(\tau, \omega) \begin{Bmatrix} x_a \\ y_a \\ z_a \end{Bmatrix} \qquad \text{Equation 3.33}$$

Now, the orientation of the cylinder determined by the coordinates $\boldsymbol{x}_{a,u}$of point a_U (Figure 3.12) with respect to the direction of the magnitude of the total velocity vector, U, were known.

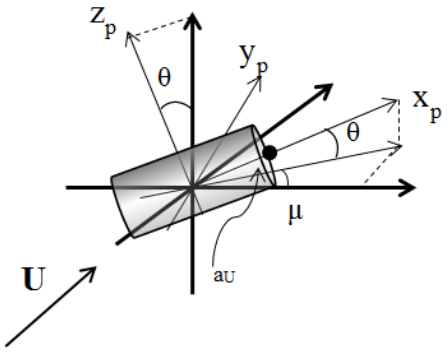

Figure 3.12 Orientation of the cylinder with respect to direction of the magnitude of the total velocity vector, U

The true pitch (θ) and yaw (μ) angles shown in Figure 3.12 were used to find the normalized aerodynamic force and moment coefficients using a linear interpolation of the plots shown in Appendix B. The forces and moments in the principle *x*-direction were then calculated using equations similar to Equation 2.32 and Equation 2.33 shown in Equation 3.34 and Equation 3.35. The forces and moments in the other principle directions can be calculated similarly.

$$F_{x,p} = C_{F_x} \frac{1}{2} \rho U^2 A_p \qquad \text{Equation 3.34}$$

$$M_{x,p} = C_{M_x} \frac{1}{2} \rho U^2 A_p D \qquad \text{Equation 3.35}$$

The projected area (*Ap*) for each combination of yaw and pitch angles was found using Equation 3.36 and Equation 3.37, where 'D' and 'L' correspond to the diameter and length of the cylinder, respectively.

$$A_p = DL\cos(\mu^*) + \pi\frac{D^2}{4}\sin(\mu^*) \qquad \text{Equation 3.36}$$

$$\mu^* = \sin^{-1}[\sin(\mu)\cos(\theta)] \qquad \text{Equation 3.37}$$

Once the force coefficients found using Equation 3.34 were calculated for the principle coordinate system, they were translated back into the global coordinate system in order to find the global acceleration of the cylinder. This was done by reversing the coordinate transformations in Equation 3.33 and Equation 3.31, as shown in Equation 3.38.

$$\begin{Bmatrix} F_x \\ F_y \\ F_z \end{Bmatrix} = \boldsymbol{R}_{y'z^*}{}^{-1}(\mu_G, \theta_G)\boldsymbol{R}_{y'z^*}(\tau, \omega)\begin{Bmatrix} F_{x,p} \\ F_{y,p} \\ F_{z,p} \end{Bmatrix} \qquad \text{Equation 3.38}$$

Unlike the sphere simulation, the cylinder simulation calculations were performed in Cartesian coordinates. The forces acting on a cylinder (neglecting force due to static pressure) at an arbitrary orientation in three-dimensional flow are shown in Figure 3.13.

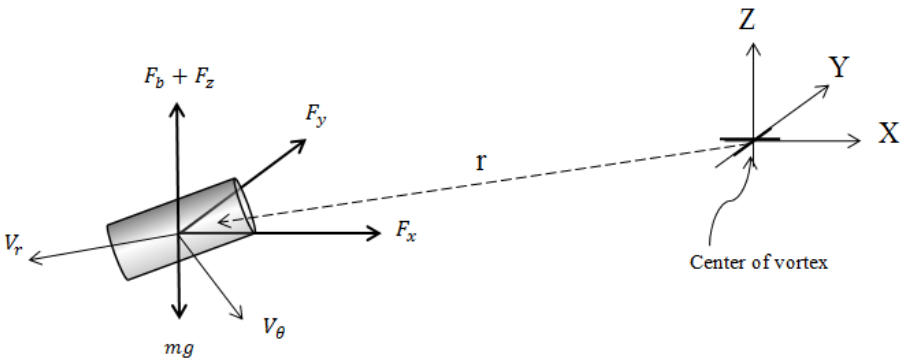

Figure 3.13 Forces acting on circular cylinder in three-dimensional flow

Based on Newton's second law, Equation 3.39 - Equation 3.43 describe the motion and rotation of the circular cylinder in three-dimensional flow in the global (*x*,*y*,*z*) coordinate

system. In Equation 3.39 and Equation 3.40, $\frac{V_\theta^2}{r}\Big|_{x,y}$ refers to the centripetal acceleration in the x- and y-direction, respectively.

$$ma_x = m\left(\frac{d^2x}{dt^2} - \frac{V_\theta^2}{r}\Big|_x\right) = F_x \quad \text{Equation 3.39}$$

$$ma_y = m\left(\frac{d^2y}{dt^2} - \frac{V_\theta^2}{r}\Big|_y\right) = F_y \quad \text{Equation 3.40}$$

$$ma_z = m\frac{d^2z}{dt^2} = F_z + F_b - mg \quad \text{Equation 3.41}$$

$$\frac{d^2\theta}{dt^2} = \frac{M_{y,p}}{I_{yy}} \quad \text{Equation 3.42}$$

$$\frac{d^2\mu}{dt^2} = \frac{M_{z,p}}{I_{zz}} \quad \text{Equation 3.43}$$

F_x, F_y, and F_z are calculated using Equation 3.38 in which:

$F_{x,p} = \frac{1}{2}\rho|U|^2 C_{Fx} A_p$ = Aerodynamic Force in x_p-direction — Equation 3.44

$F_{y,p} = \frac{1}{2}\rho|U|^2 C_{Fy} A_p$ = Aerodynamic Force in y_p-direction — Equation 3.45

$F_{z,p} = \frac{1}{2}\rho|U|^2 C_{Fz} A_p$ = Aerodynamic Force in z_p-direction — Equation 3.46

$F_b = \rho g \frac{1}{6}\pi D^3$ = Buoyancy Force — Equation 3.47

$M_{y,p} = \frac{1}{2}\rho|U|^2 C_{My} A_p D$ = Aerodynamic Moment about y_p -direction — Equation 3.48

$M_{z,p} = \frac{1}{2}\rho|U|^2 C_{Mz} A_p D$ = Aerodynamic Moment about z_p -direction — Equation 3.49

$I_{yy} = \frac{1}{12} m\left[3\left(\frac{D}{2}\right)^2 + l^2\right]$ = Moment of inertia along the y_p-direction — Equation 3.50

$I_{zz} = \frac{1}{12} m \left[3 \left(\frac{D}{2} \right)^2 + l^2 \right]$ = Moment of inertia along the z_p-direction Equation 3.51

3.2.3.2 Validation of Cylinder Forces

The validation procedure of the cylinder forces was similar to the validation procedure used for the sphere as described in section 3.2.2.2. A circular cylinder of aspect ratio of 3:1 (length:diameter) was hung from the center of the tornado simulator by a string of length *l*, and when the tornado simulator was turned on the cylinder reached an equilibrium spinning at a certain r and h depending on the object properties, length *l* of string, and the swirl ratio of the vortex. The height *h* was measured manually in the experiment, and the radius *r* was calculated from that. The goal in this validation test was to accurately calculate the height and radius at which the cylinder will reach equilibrium for various swirl ratios. The same low swirl ratios were used for these tests (0.08-0.24) as for the sphere forces validation tests. However, it is believed that the force equations can be used in any swirl ratio.

One cylinder was used in this experiment of diameter 44.5 mm (1.75 inch) and length 133.4 mm (5.25 inches). Weights were added to the cylinder so that the experiment was performed for three different masses: 6.3, 11.4, and 16.4 g.

Since the cylinder was in equilibrium in the radial plane, the forces were analyzed in the global coordinate system at (x,y) = (-r,0), where r is the radial location of the center of the cylinder. At this location, the relationship between velocity components in the Cartesian and radial coordinate systems is given by Equation 3.52

$$\begin{Bmatrix} V_x \\ V_y \\ V_z \end{Bmatrix} = \begin{Bmatrix} -V_r \\ -V_\theta \\ V_z \end{Bmatrix} \quad \text{Equation 3.52}$$

The forces acting on the cylinder when tied to a string are shown in Figure 3.14, where $\theta_G = \alpha$ and $\mu_G = 0$ as described in Figure 3.10.

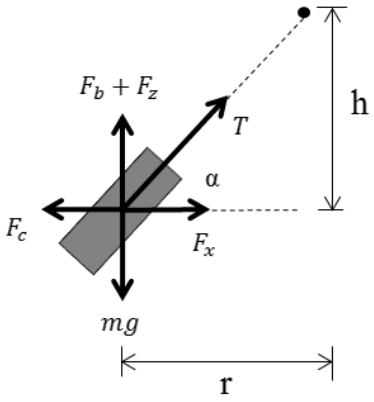

Figure 3.14 Forces acting on a cylinder in the validation test

The forces were calculated as shown in Equation 3.44 to Equation 3.47. The acceleration component, $\frac{d^2x}{dt^2}$, in the horizontal direction and a_z in the vertical direction were set to zero, shown in Equation 3.53 and Equation 3.55, and substituted into Equation 3.39 and Equation 3.41. The equilibrium equations are shown in Equation 3.54 and Equation 3.56, where T is the tension force in the string.

$$\frac{d^2x}{dt^2} = 0 \quad \text{Equation 3.53}$$

$$T\cos\alpha = F_c - F_x \quad \text{Equation 3.54}$$

$$\frac{d^2z}{dt^2} = 0 \quad \text{Equation 3.55}$$

$$T\sin\alpha = mg - F_b - F_z \quad \text{Equation 3.56}$$

Equation 3.54 and Equation 3.56 were combined by solving for T. The resulting equation is shown in Equation 3.57.

$$(F_c - F_x)\tan\alpha + F_b + F_z - mg = 0 \qquad \text{Equation 3.57}$$

Equation 3.26 and Equation 3.28 were substituted into Equation 3.57 to give Equation 3.58, which was solved for *r*.

$$r^2[F_b + F_z - mg] - r[hF_x] + hmV_\theta^2 = 0 \qquad \text{Equation 3.58}$$

This final equation is quadratic for *r*, however it includes *h* and all the forces are functions of *r* and *h*. For this reason, the equation was solved iteratively. The resulting calculated *r* for each cylinder mass and various swirl ratios and fan speeds were compared with actual measured *r* in Table 3.3. Plots of velocity and pressure measurements for the various swirl ratios and fan speeds can be found in Appendix C.

Table 3.3 Results of the cylinder forces validation test

						Actual	Calculated	
Length (mm)	Mass (g)	Swirl Ratio	$V_{\theta,max}$ (m/s)	h (mm)	l (mm)	r (mm)	r (mm)	%diff
133.4	11.4	0.08	2.04	699	756	434	430	0.84
			1.97	483	546	393	407	3.41
			2.95	483	635	509	519	1.96
	16.4		1.97	457	533	389	396	1.98
			2.04	724	775	429	436	1.62
			2.95	483	641	518	513	1.01
	6.3		2.04	457	533	389	411	5.80
			3.07	470	635	521	531	1.92
		0.24	1.89	737	864	568	533	6.21
			2.66	737	953	704	691	1.91

The percent difference between calculated *r* and the actual measured *r* value is less than 10% for all cases. This experimental error is considered acceptable and shows that the forces used in calculations accurately model the forces acting on the cylinder.

CHAPTER 4. RESULTS AND DISCUSSION

4.1 COMPARISON OF EXPERIMENTAL AND NUMERICAL TRAJECTORIES

4.1.1 Sphere

Table 2.5 gives parameters of the trajectory tests where Tests 1 to 4 correspond to the sphere debris objects. The three-dimensional plots of the experimentally observed and numerically simulated trajectories of the sphere for Tests 1 to 4 are given in Figure 4.1 - Figure 4.4. Radial location of the debris object refers to the distance between the origin of the (x,y,z) coordinate system along the axis of the vortex (Figure 3.13) and the center of the debris object. Radial locations of the experimental trajectories were calculated for times corresponding to the frames used. The locations of the numerically simulated trajectories were calculated at very small time steps (0.0035sec), but only the radial location at those time steps corresponding to the experimental time steps were used in the comparison. Velocities of the experimental trajectories were found by taking the distance traveled between two frames and multiplying by the frame rate, in this case 30 fps. Comparisons of numerically simulated vs. experimental conditions for the sphere debris are given in Table 4.1 - Table 4.4, until the time when either trajectory impacted the ground. The percent difference shown was calculated with respect to the experimental trajectory.

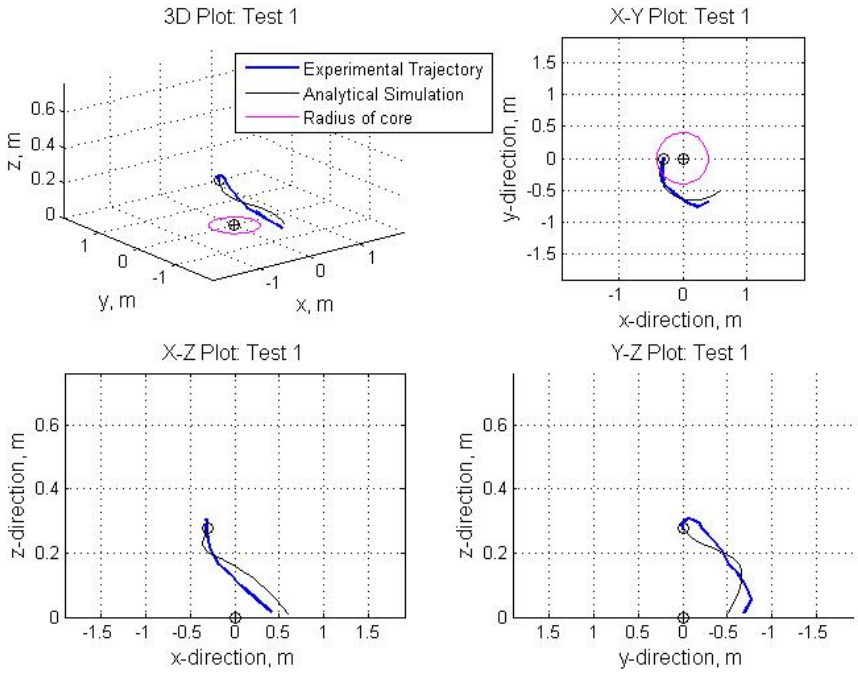

Figure 4.1 Comparison of experimental vs. numerically simulated sphere trajectory, Test 1 (r_0 = 305mm, h_0 = 279.5mm)

Table 4.1 Trajectory comparisons for Test 1

	Time	Experimental	Numerical	% diff
Radial location (m)	0.000	0.412	0.413	0.3
	0.035	0.427	0.414	3.1
	0.067	0.443	0.416	5.9
	0.102	0.453	0.421	7.0
	0.133	0.470	0.428	9.1
	0.168	0.478	0.439	8.1
	0.200	0.515	0.453	11.9
	0.235	0.550	0.475	13.7
	0.266	0.568	0.498	12.2
	0.301	0.630	0.527	16.3
	0.333	0.719	0.555	22.8
	0.368	0.804	0.589	26.8
Final Time (s)		0.400	0.574	30.3
Final Velocity (m/s)		5.607	5.164	7.9

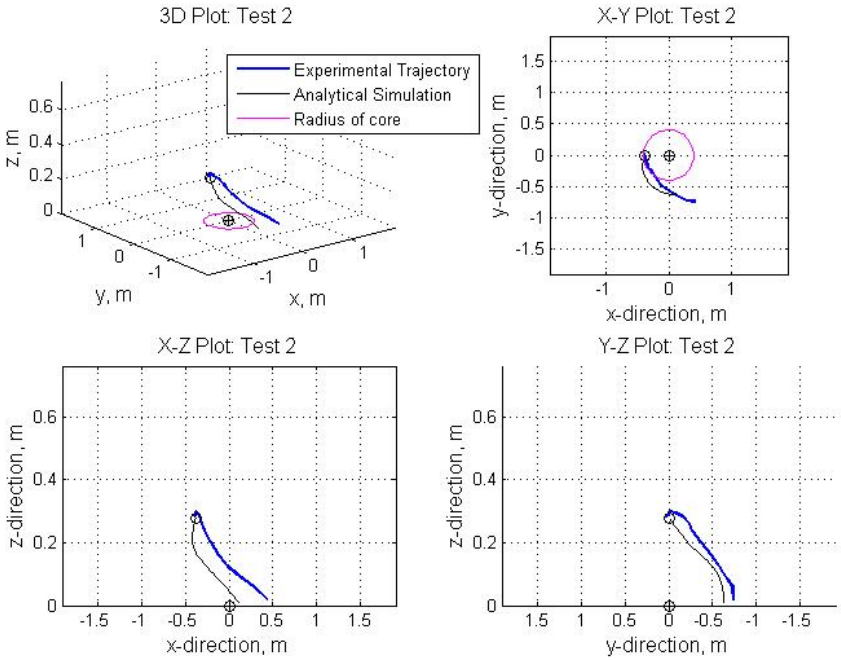

Figure 4.2 Comparison of experimental vs. numerically simulated sphere trajectory, Test 2 (r_0 = 381mm, h_0 = 279.5mm)

Table 4.2 Trajectory comparisons for Test 2

	Time	Experimental	Numerical	% diff
Radial location (m)	0.000	0.488	0.472	3.2
	0.035	0.479	0.473	1.3
	0.067	0.487	0.474	2.6
	0.102	0.486	0.477	2.0
	0.133	0.473	0.480	1.4
	0.168	0.472	0.486	3.0
	0.200	0.466	0.493	5.9
	0.235	0.448	0.503	12.2
	0.266	0.467	0.514	10.2
	0.301	0.525	0.532	1.4
	0.333	0.584	0.552	5.5
	0.368	0.669	0.575	14.0
	0.399	0.780	0.597	23.5
Final Time (s)		0.433	0.462	6.6
Final Velocity (m/s)		4.839	4.635	4.2

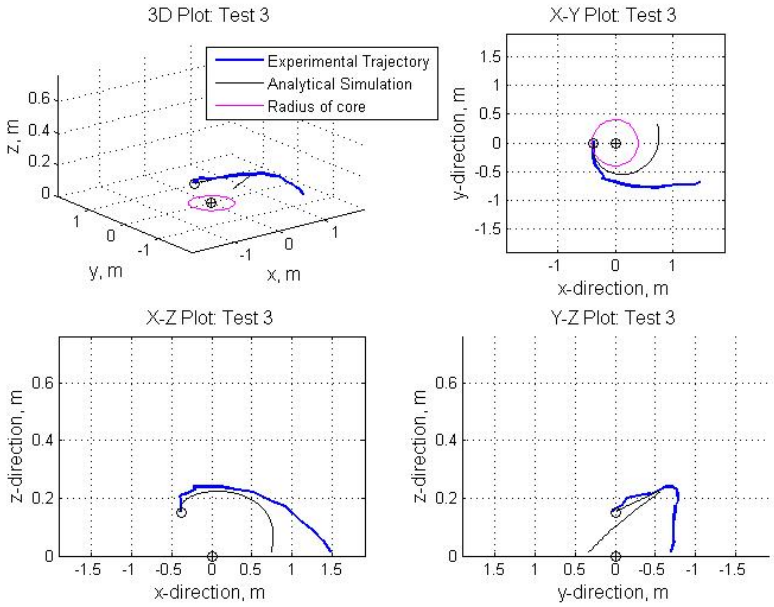

Figure 4.3 Comparison of experimental vs. numerically simulated sphere trajectory, Test 3 (r_0 = 381mm, h_0 = 152.5mm)

Table 4.3 Trajectory comparisons for Test 3

	Time	Experimental	Numerical	% diff
Radial location (m)	0.000	0.417	0.410	1.6
	0.035	0.415	0.419	0.9
	0.067	0.426	0.438	2.9
	0.102	0.455	0.469	3.1
	0.133	0.489	0.503	2.9
	0.168	0.560	0.543	3.0
	0.200	0.584	0.578	0.9
	0.235	0.650	0.615	5.4
	0.266	0.711	0.645	9.3
	0.301	0.764	0.677	11.4
	0.333	0.856	0.704	17.8
	0.368	0.959	0.733	23.6
	0.399	1.077	0.758	29.6
	0.434	1.192	0.786	34.0
Final Time (s)		0.567	0.462	18.5
Final Velocity (m/s)		3.312	5.779	74.5

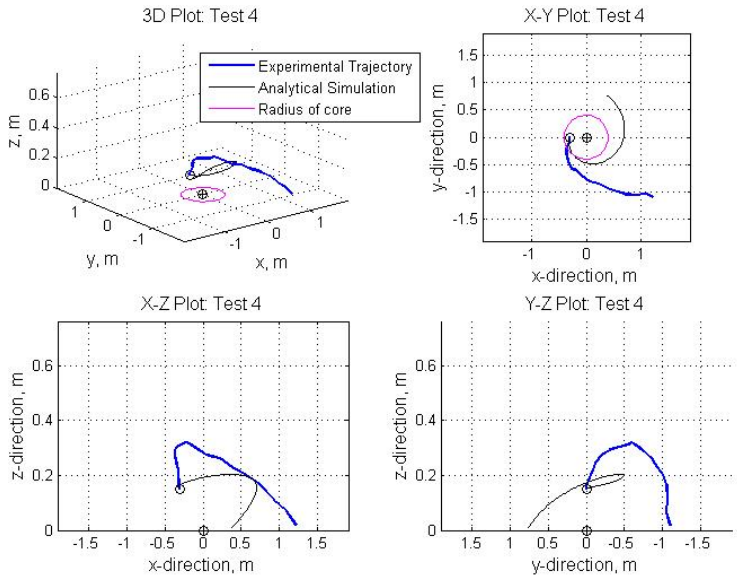

Figure 4.4 Comparison of experimental vs. numerically simulated sphere trajectory, Test 4 (r_0 = 305mm, h_0 = 152.5mm)

Table 4.4 Trajectory comparisons for Test 4

	Time	Experimental	Numerical	% diff
Radial location (m)	0.000	0.343	0.341	0.6
	0.035	0.356	0.347	2.4
	0.067	0.398	0.362	9.1
	0.102	0.439	0.387	11.9
	0.133	0.505	0.416	17.7
	0.168	0.561	0.455	18.9
	0.200	0.633	0.495	21.9
	0.235	0.708	0.541	23.6
	0.266	0.704	0.583	17.1
	0.301	0.774	0.628	18.8
	0.333	0.862	0.666	22.7
	0.368	0.914	0.706	22.8
	0.399	1.030	0.740	28.2
	0.434	1.167	0.777	33.4
	0.466	1.298	0.809	37.7
	0.501	1.407	0.843	40.0
Final Time (s)		0.567	0.508	10.4
Final Velocity (m/s)		4.188	6.432	53.6

4.1.2 Cylinder

Table 2.5 gives the parameters of the trajectory tests (Tests 5 and 6) for the cylinder debris objects. The validation experiment performed in section 3.2.3.2 showed that the force coefficients extracted from the wind tunnel tests along with the method to predict the trajectory was accurate. However, there was no way to accurately validate the moment coefficient and moment equations. Therefore, the cylinder trajectory numerical simulation was performed for a non-rotating cylinder. Figure 4.5 and Figure 4.6 are three-dimensional plots of the experimental vs. numerically simulated cylinder trajectories that include all forces described in section 3.2.3 with static global pitch (θ_G) and yaw (μ_G) angles of zero, which means that the cylinder axis was always aligned along the global x-direction and lies in the horizontal plane.

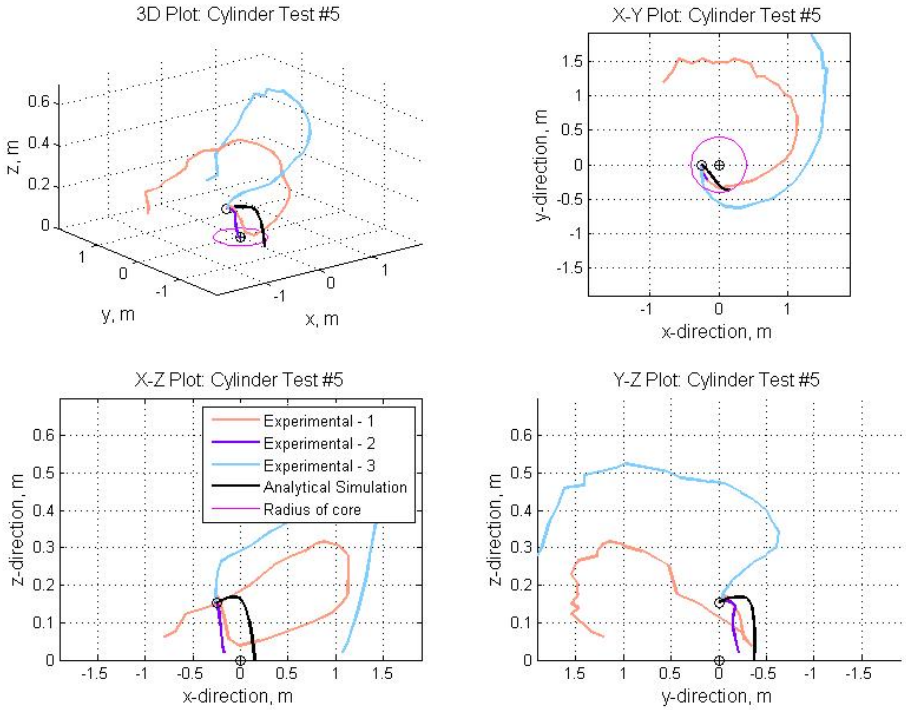

Figure 4.5 Comparison of experimental vs. numerically simulated sphere trajectory, Test 5 (r_0 = 254mm, h_0 = 152.5mm)

Table 4.5 Trajectory comparisons for Test 5

	Time	Experimental	Numerical	% diff
Radial location (m)	0.000	0.299	0.296	0.8
	0.035	0.305	0.266	12.7
	0.067	0.323	0.248	23.4
	0.102	0.342	0.290	15.0
	0.133	0.368	0.366	0.5
	0.168	0.373	0.399	7.1
Final Time (s)		0.267	0.168	37.0
Final Velocity (m/s)		5.716	9.677	69.3

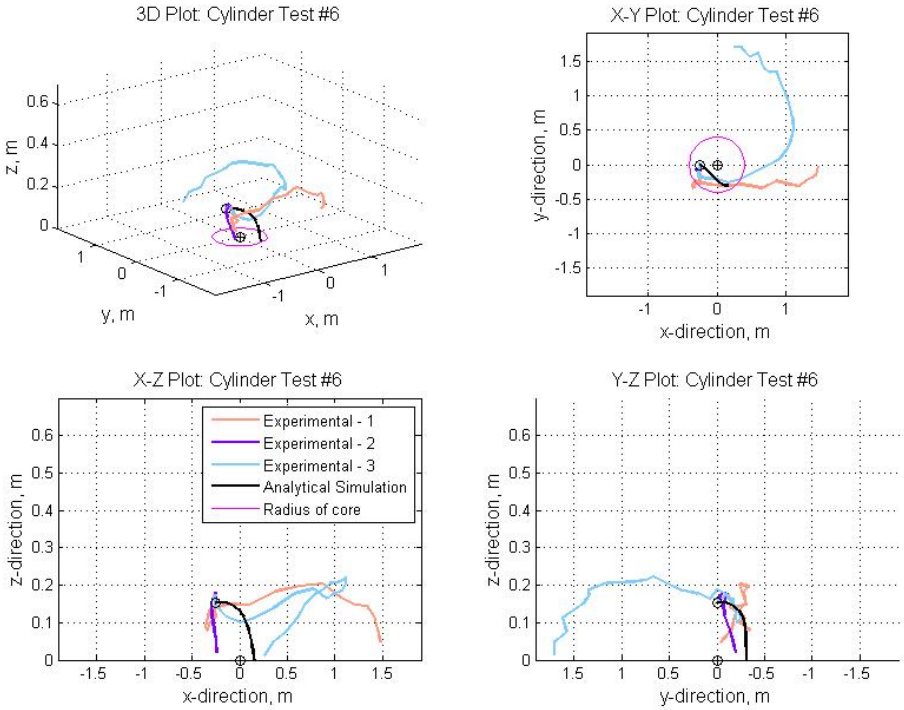

Figure 4.6 Comparison of experimental vs. numerically simulated sphere trajectory, Test 6 (r_0 = 254mm, h_0 = 152.5mm)

Table 4.6 Trajectory comparisons for Test 6

	Time	Experimental	Numerical	% diff
Radial location (m)	0.000	0.302	0.296	1.9
	0.035	0.307	0.274	10.6
	0.067	0.322	0.239	26.0
	0.102	0.333	0.224	32.7
	0.133	0.343	0.252	26.5
	0.168	0.334	0.311	7.0
	0.200	0.300	0.340	13.6
Final Time (s)		0.300	0.200	33.5
Final Velocity (m/s)		2.072	5.402	160.7

4.2 DISCUSSION OF RESULTS

The forces defining the movement of both the sphere and cylinder debris objects were validated for low swirl ratios ('Vane 1' and 'Vane 3' settings) as described in sections 3.2.2.2 and 3.2.3.2. The numerical results matched the experimental results very well in controlled-flight, which leads to the conclusion that the forces acting on the objects in the ISU Tornado Simulator were accurately modeled in the numerical analysis for those swirl ratios. The free-flight trajectory of the debris objects were modeled numerically and measured experimentally in a tornado-like vortex of a larger swirl ratio ('Vane 5' setting). However, one property of vortices with large swirl ratios is high turbulence content. Figure 4.7 shows the turbulence intensity of the total velocity component for the 'Vane 5 setting' vortex.

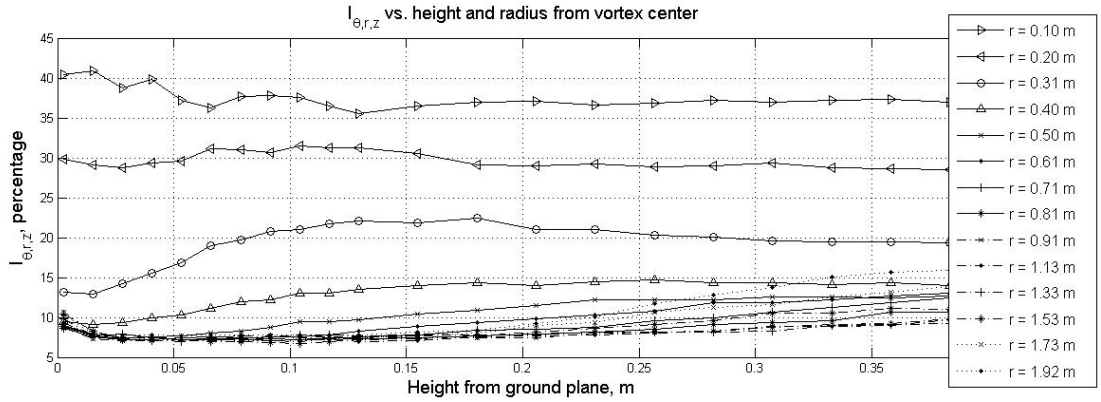

Figure 4.7 Turbulence intensity of total velocity component for 'Vane 5' setting

As shown in the figure, turbulence is greater inside the core ($r \leq r_c = 0.40$ m) than outside. As noted in section 3.1, the numerical simulation did not account for turbulence at all in the generated velocity field. Therefore, any error in the simulation model due to calculation of only mean velocity was cumulative because the velocity field was calculated based on the current location of the object and force prediction was dependent on relative velocity of the

object at each time step. Including turbulence in the model would take into account perturbation of velocity from the mean and would create a broader “window” of simulations that could more accurately model the experimental trajectories.

Figure 4.1 - Figure 4.4 show that the numerical simulation was fairly accurately capturing the trend of the free-flight experimental trajectories for the spherical debris case. It seems as though the tests where the initial height was higher (Test 1 and Test 2) exhibited more accurate numerical simulations than Test 3 and Test 4, where the initial height was lower. The debris object used in Test 2 had different length and mass properties than the object used in the other three tests, yet the comparison between the numerical and experimental trajectories was not significantly different. Therefore, this methodology can be used with any object of reasonable mass and length properties, and numerical trajectories similar to experimental trajectories could be expected. It is clear looking at Table 4.1- Table 4.4 that as time increases, so does the amount of error in radial location between numerical and experimental trajectories. In Tests 1 and 2 the error in both radial location and final velocity was much lower than Tests 3 and 4, leading to the conclusion that a higher initial height gives more accurate numerical results.

As debris objects become three-dimensional, the complexity of the numerical simulation increases. This is shown in the cylinder Tests 5 and 6 in Figure 4.5 and Figure 4.6. The numerical trajectory is compared with an average of all three experimental trajectories in Table 4.5 and Table 4.6. Even with the complexity of the model and the assumptions used, the numerical simulations exhibited a similar trend to the experimental trajectories as shown in the tables. In numerical simulation of the cylinder trajectory, the rotational motion from

moment was neglected to simplify the equations of motion, and therefore the cylinder orientation was maintained stationary in the global coordinate system throughout the trajectory. Since the error due to the velocity model was cumulative as described earlier, the numerical simulation did not match well with the experimental trajectories in the later part of the debris flight. However, the error between the numerical and experimental trajectories was low at the beginning of the trajectories (for the first few time steps). This could be due to the fact that in the mathematical models, the cylinder orientation at the beginning of the trajectories was very similar to the experimental cases.

CHAPTER 5. CONCLUSION

5.1 SUMMARY AND CONCLUSIONS OF CURRENT WORK

Experimental and numerical studies of the trajectory of simplified debris objects in a three-dimensional tornadic flow field were performed. The summary and conclusions made from the results are as follows:

- A stereo-photogrammetry method was developed for use in ISU's Tornado Simulator as described in section 2.1.1 which does not require the use of high-speed cameras or other expensive equipment. The validation experiment described in section 2.1.2 shows that the method developed is accurate to within 3% in both the horizontal and vertical frames as tested. The method can be used for any number of research experiments in the tornado simulator, including various swirl ratios, terrain conditions, vortex structures, and even translating tornadoes as long as the object is always viewable by both cameras.
- The forces acting on a sphere-like object and circular cylinder-like object were developed as described in section 3.2. Forces due to buoyancy, static pressure, and centripetal acceleration were included in the numerical model in addition to aerodynamic forces. The forces were validated using an experiment similar to that used in the stereo-photogrammetry validation test, where an object of known mass and length properties was suspended by a string from the center of the tornado

simulator. The object reached equilibrium spinning at a specific height and radius dependent on the vortex properties. This radius at which the object reached equilibrium was calculated based on the forces acting on the object and compared to the measured radius. The comparison between the observed- and numerically-simulated trajectories for both the sphere and cylinder in controlled-flight condition was quite good (the difference between predicted and measured radius was consistently within 10%) and this validated the equations used to model forces acting on the objects.

- All the forces acting on the sphere and circular cylinder, as described in section 3.2, were used to numerically simulate free-flight trajectories in ISU's Tornado Simulator. A velocity program written by Thampi (2010) was modified and used to calculate the velocity field generated by the simulator. A constant acceleration integration method was used to propagate the trajectories of various objects. In the numerically-simulated free-flight trajectory of the cylinder, the effects of moment and angular accelerations were neglected to simplify the equations of motion. The cylinder experimental trajectory was performed three times and the average of those trajectories were compared with numerical simulation. The error between the observed- and numerically-simulated trajectories for both the sphere and cylinder in free-flight was low at the beginning of flight and increased with time.

5.2 RECOMMENDATIONS FOR FUTURE RESEARCH

In order to improve the comparison between the numerically-simulated and experimental trajectories for both the sphere and cylinder debris objects, turbulence intensity from Figure 4.7 could be included into the velocity model in section 3.1. This would take into account perturbation of velocity from the mean and would create a broader “window” of simulations that could more accurately model the experimental trajectories. In the future, the moment equations could also be included into the numerical simulation in order to further improve accuracy the numerically-simulated cylinder trajectory.

The methodology described in this work could be expanded to different cases by using different sizes and masses of debris object as well as changing the initial conditions for the free-flight trajectories.

APPENDIX A. STEREO-PHOTOGRAMMETRY TRAJECTORIES

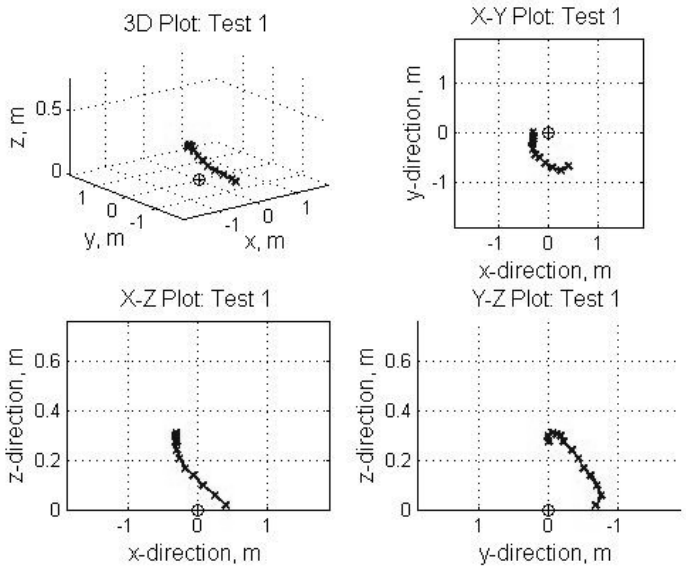

Figure A.1 Stereo-photogrammetry trajectory, Test 1

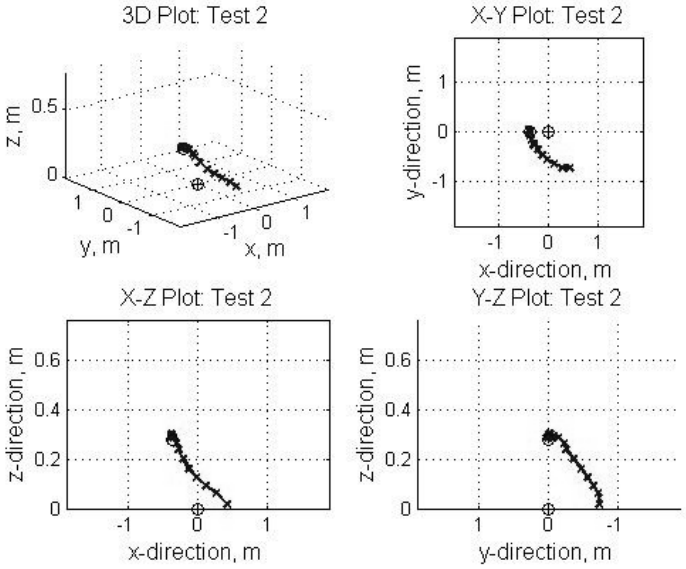

Figure A.2 Stereo-photogrammetry trajectory, Test 2

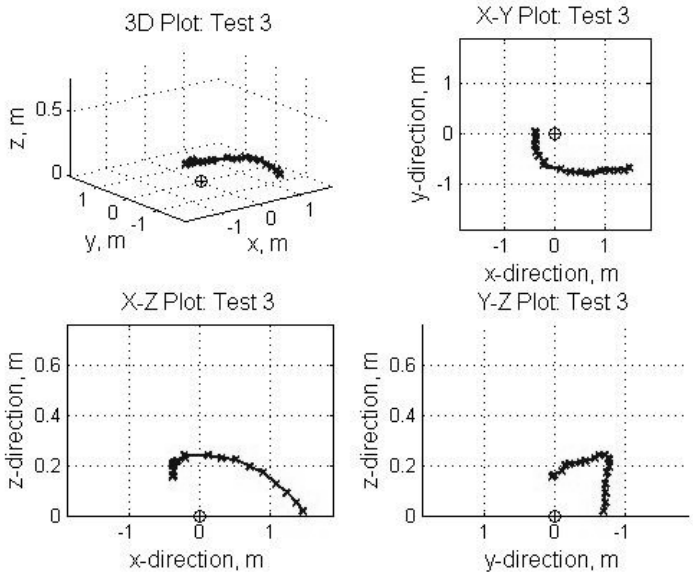

Figure A.3 Stereo-photogrammetry trajectory, Test 3

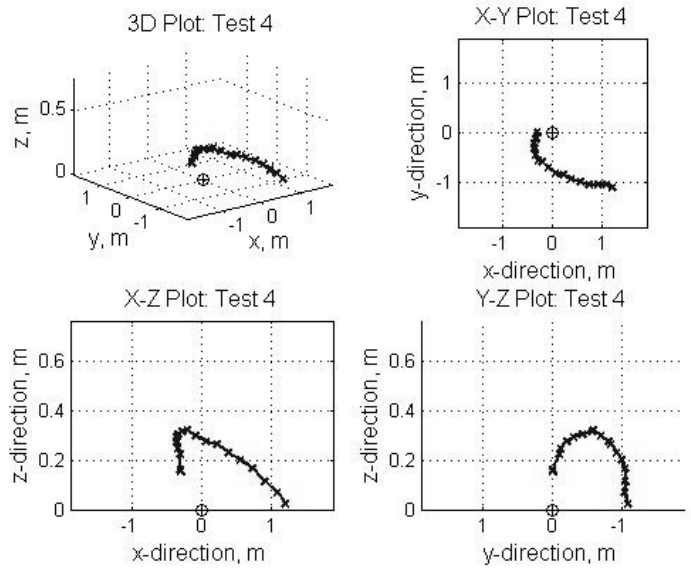

Figure A.4 Stereo-photogrammetry trajectory, Test 4

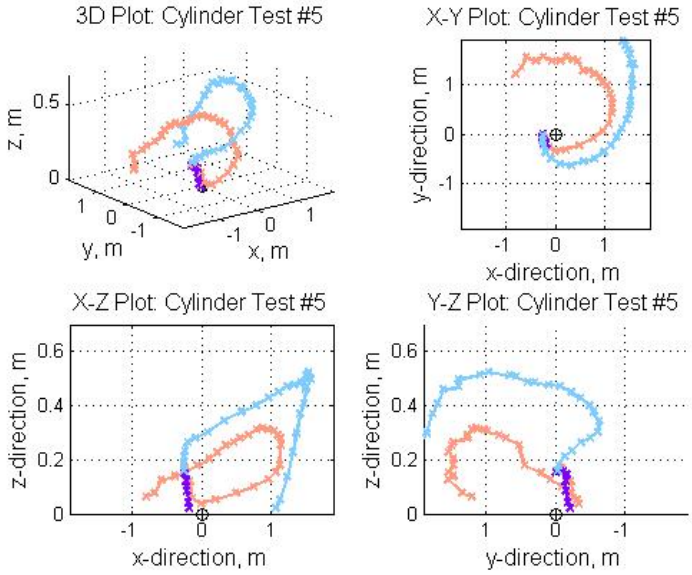

Figure A.5 Stereo-photogrammetry trajectory, Test 5

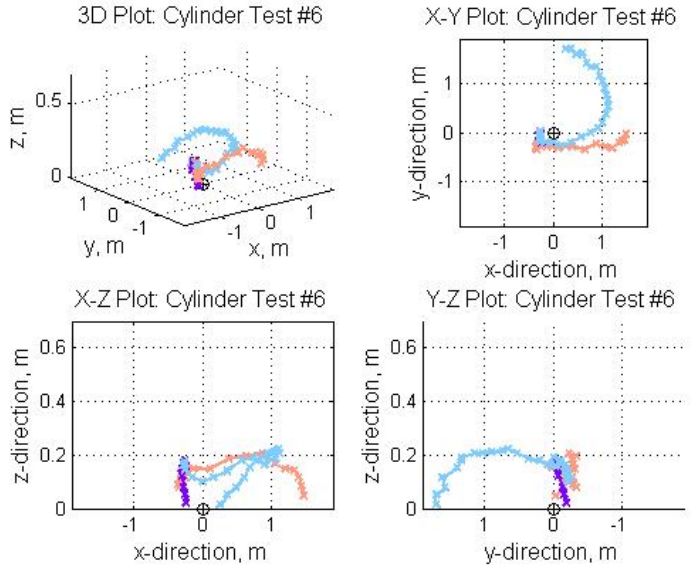

Figure A.6 Stereo-photogrammetry trajectory, Test 6

APPENDIX B. COEFFICIENTS OF CIRCULAR CYLINDER

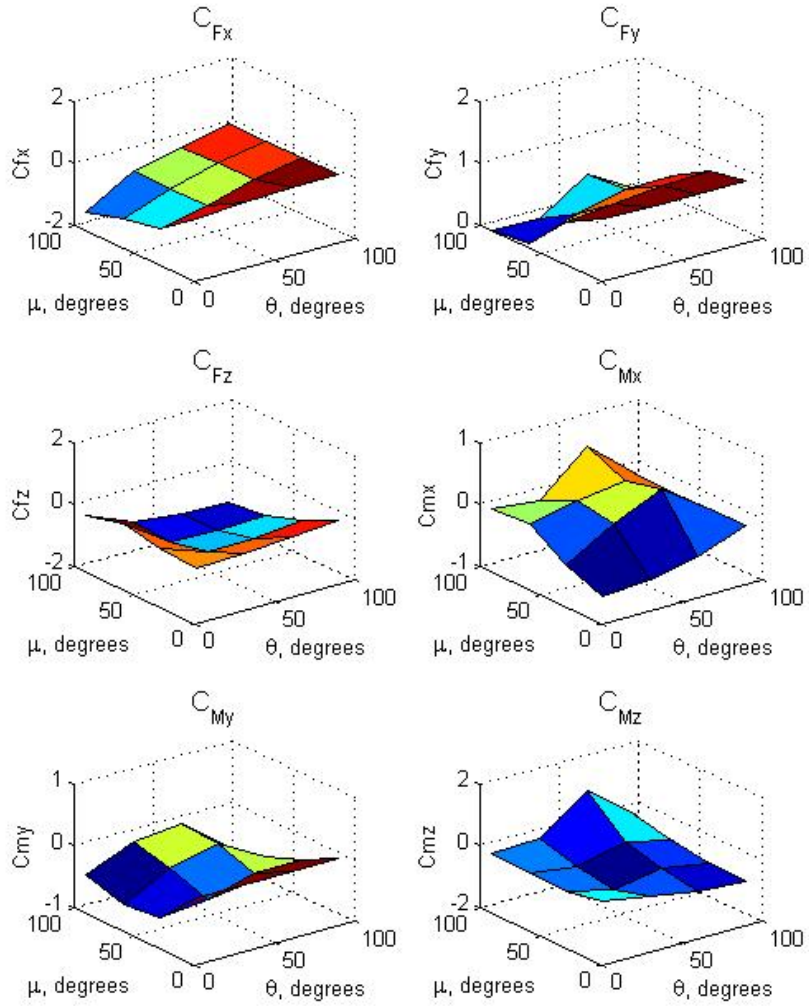

Figure A.7 Coefficients of circular cylinder, calculated from data collected in Bill James Wind Tunnel

APPENDIX C. VELOCITY AND PRESSURE MEASUREMENT PLOTS

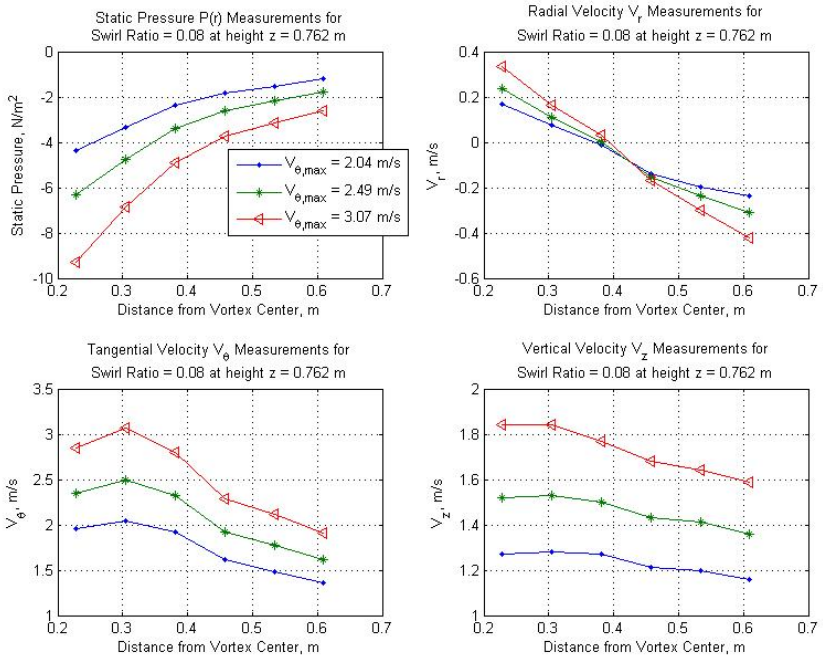

Figure A.8 Pressure and velocity measurements for swirl ratio = 0.08 and height z = 0.762 m

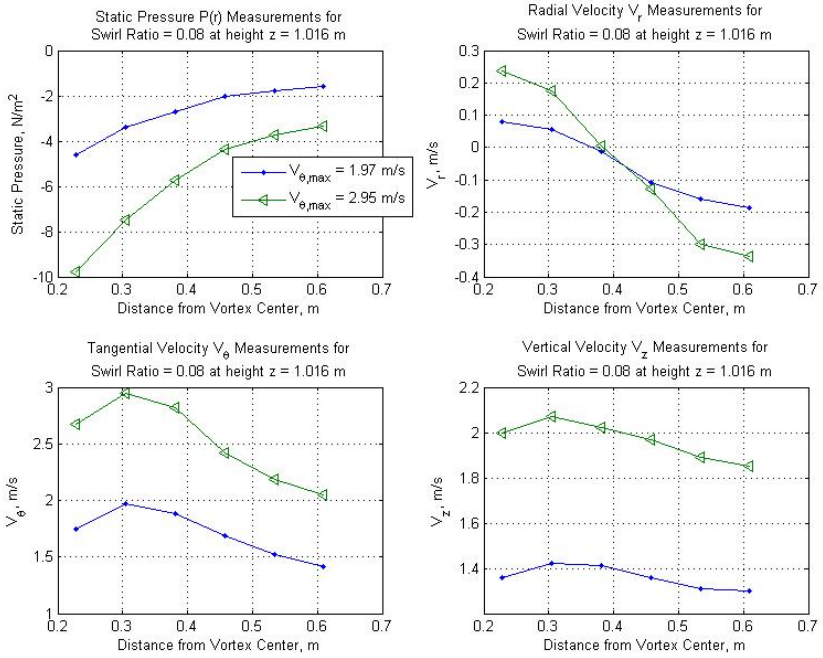

Figure A.9 Pressure and velocity measurements for swirl ratio = 0.08 and height z = 1.016 m

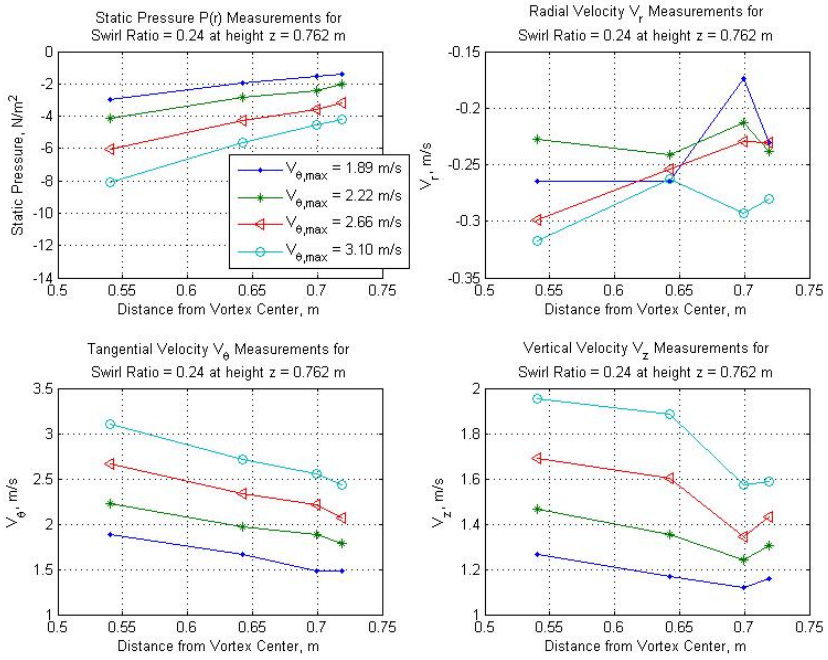

Figure A.10 Pressure and velocity measurements for swirl ratio = 0.24 and height z = 0.762 m

BIBLIOGRAPHY

Baker, C. (2007). The debris flight equations. *Journal of Wind Engineering and Industrial Aerodynamics*, 329-353.

Blevins, R. D. (1992). *Applied fluid dynamics handbook.* Malabar, Florida: Krieger Publishing Company.

Davies-Jones, R. (1973). The dependence of core radius on swirl ratio in a tornado simulator. *Journal of the Atmospheric Sciences, 30*, 1427-1430.

Dowell, D. C., Alexander, C. R., Wurman, J. M., & Wicker, L. J. (2005). Centrifuging of hydrometeors and debris in tornadoes: radar-reflectivity patterns and wind-measurement errors. *American Meteorological Society*, 1501-1524.

Haan Jr., F. L., Sarkar, P. P., & Gallus, W. A. (2008, April). Design, construction and performance of a large tornado simulator for wind engineering applications. *Engineering Structures, 30*(4), 1146-1159.

Holmes, J. (2004). Trajectories of spheres in strong winds with application to wind-borne debris. *Journal of Wind Engineering and Industrial Aerodynamics*, 9-22.

Holmes, J., Letchford, C., & Lin, N. (2006). Investigations of plate-type windborne debris, part II computed trajectories. *Journal of Wind Engineering and Industrial Aerodynamics*, 21-39.

Kordi, B., & Kopp, G. A. (2009). "The debris flight equations" by C.J. Baker. *Journal of Wind Engineering and Industrial Aerodynamics*, 151-154.

Kordi, B., & Kopp, G. A. (2009). Evaluation of quasi-steady theory applied to windborne flat plates in uniform flow. *Journal of Engineering Mechanics*, 657-668.

Kordi, B., & Kopp, G. A. (2011). Effects of initial conditions on the flight of windborne plate debris. *Journal of Wind Engineering and Industrial Aerodynamics*, 601-614.

Lin, N., Holmes, J. D., & Letchford, C. W. (2007). Trajectories of wind-borne debris in horizontal winds and applications to impact testing. *Journal of Structural Engineering*, 274-282.

Lin, N., Letchford, C., & Holmes, J. (2006). Investigation of plate-type windborne debris, part I experiments in wind tunnel and full scale. *Journal of Wind Engineering and Industrial Aerodynamics*, 51-76.

Maruyama, T. (2011). Simulation of flying debris using a numerically generated tornado-like vortex. *Journal of Wind Engineering and Industrial Aerodynamics*, 249-256.

McDonald, J. R. (1976). Tornado-generated missiles and their effects. *Proceedings of the Symposium on Tornadoes: Assessment of Knowledge and Implications for Man*, 331-348.

McDonald, J. R. (1990). Impact resistance of common building materials to tornado missiles. *Journal of Wind Engineering and Industrial Aerodynamics, 36*, 717-724.

Minor, J. E. (1994). Windborne debris and the building envelope. *Journal of Wind Engineering and Industrial Aerodynamics, 53*, 207-227.

Sarkar, P. P., & Kikitsu, H. (2009). Experimental studies on internal pressure and debris strike for improved tornado induced loads of low-rise buildings. *Proceedings of the 41st US-Japan Panel on Wind and Seismic Effects Joint Meeting.* Gaithersburg, MD.

Tachikawa, M. (1983). Trajectories of flat plates in uniform flow with application to wind-generated missiles. *Journal of Wind Engineering and Industrial Aerodynamics*, 443-453.

Tachikawa, M. (1988). A method for estimating the distribution range of trajectories of wind-borne missiles. *Journal of Wind Engineering and Industrial Aerodynamics*, 175-184.

Thampi, H. (2010). Interaction of a translating tornado with a low-rise building. *Master's Thesis in Aerospace Engineering*. Ames, IA: Iowa State University.

Visscher, B. T., & Kopp, G. A. (2007). Trajectories of roof sheathing panels under high winds. *Journal of Wind Engineering and Industrial Aerodynamics*, 697-713.